Millennial to orbital-scale variations of drought intensity in the Eastern Mediterranean

Mona Stockhecke [a, b, c, *], Axel Timmermann [d, **], Rolf Kipfer [e, f, g], Gerald H. Haug [b], Ola Kwiecien [e, h], Tobias Friedrich [d], Laurie Menviel [i, j], Thomas Litt [k], Nadine Pickarski [k], Flavio S. Anselmetti [c, l, m]

[a] Large Lakes Observatory, University of Minnesota Duluth, 10 University Drive 206 RLB, Duluth, MN, 55812-2496, USA
[b] Geological Institute, Swiss Federal Institute of Technology (ETH), Sonneggstrasse 5, 8092, Zürich, Switzerland
[c] Eawag, Swiss Federal Institute of Aquatic Science and Technology, Department of Surface Waters Research and Management, Überlandstrasse 133, 8600, Dübendorf, Switzerland
[d] IPRC, and Department of Oceanography, SOEST, 1680 East-West Road, University of Hawaii, Honolulu, 96822, HI, USA
[e] Eawag, Swiss Federal Institute of Aquatic Science and Technology, Department of Water Resources and Drinking Water, Überlandstrasse 133, 8600, Dübendorf, Switzerland
[f] Institute of Biogeochemistry and Pollutant Dynamics, Swiss Federal Institute of Technology (ETH), Universitätstrasse 16, 8092, Zürich, Switzerland
[g] Institute of Geochemistry and Petrology, Swiss Federal Institute of Technology (ETH), Clausiusstrasse 25, 8092, Zürich, Switzerland
[h] Ruhr-University Bochum, Universitätsstrasse 150, 44801, Bochum, Germany
[i] CCRC, University of New South Wales, Matthews Building Level 4, Sydney, NSW, 2052, Australia
[j] ARC Centre of Excellence for Climate System Science, Australia
[k] Steinmann Institute of Geology, Mineralogy and Paleontology, Bonn University, Nussallee 8, 53115, Bonn, Germany
[l] Institute of Geological Sciences, University of Bern, Baltzerstrasse 1+3, 3012, Bern, Switzerland
[m] Oeschger Centre for Climate Change Research (OCCR), University of Bern, Switzerland

ARTICLE INFO

ABSTRACT

Millennial to orbital-scale rainfall changes in the Mediterranean region and corresponding variations in vegetation patterns were the result of large-scale atmospheric reorganizations. In spite of recent efforts to reconstruct this variability using a range of proxy archives, the underlying physical mechanisms have remained elusive. Through the analysis of a new high-resolution sedimentary section from Lake Van (Turkey) along with climate modeling experiments, we identify massive droughts in the Eastern Mediterranean for the past four glacial cycles, which have a pervasive link with known intervals of enhanced North Atlantic glacial iceberg calving, weaker Atlantic Meridional Overturning Circulation and Dansgaard-Oeschger cold conditions. On orbital timescales, the topographic effect of large Northern Hemisphere ice sheets and periods with minimum insolation seasonality further exacerbated drought intensities by suppressing both summer and winter precipitation.

1. Introduction

Rapid climate shifts between North Atlantic cold (stadial) and warm (interstadial) states occurred frequently during past glacial periods (Bond et al., 1993; Capron et al., 2010; Deplazes et al., 2013; Grützner and Higgins, 2010; Menviel et al., 2014). This continuum of variability, referred to as Dansgaard-Oeschger (DO) variability, was closely related to the presence or absence of ice-rafted debris (IRD) layers in the North Atlantic (Hemming, 2004; Hodell et al., 2008; McManus et al., 1999) or in the Nordic Seas (Bond et al., 1993; van Kreveld et al., 2000). IRD layers mark periods of enhanced iceberg calving and freshwater discharge from the major glacial ice sheets. Various high-resolution paleo-proxy datasets document that the ratio between the length of DO interstadials and stadials was strongly modulated by the ice-sheet sizes (Schulz, 2002) and the precession cycle (Timmermann et al., 2010).

One key region that exhibits particularly strong hydroclimate sensitivity to both DO and orbital-scale variability is the Eastern

Mediterranean region (Bartov et al., 2003; Daniau et al., 2007; Fleitmann et al., 2009; Harrison and Goñi, 2010; Penaud et al., 2011; Tzedakis et al., 2006; Van Meerbeeck et al., 2011; among others). Under present-day conditions, precipitation peaks in Eastern Turkey in April and in October/November, with a hot and dry summer season separating the two seasonal precipitation maxima (Fig. 1A, B). The semi-annual cycle is a characteristic feature of high-elevation regions. South-easterly wind dominates in spring likely transporting moisture from the Caspian or Arabian Sea into the area, while south-westerly winds dominate during fall and moisture from the Mediterranean Sea precipitates (Wind vector data from Climate Prediction Centre USA, http://iridl.ldeo.columbia.edu).

Based on the available meteorological data from Van (1949—2013), the total annual precipitation amounts to 389 mm and monthly mean air temperatures varies between 22.1 °C and −3.6 °C with an annual mean of 9.1 °C. Summer aridity results from large-scale subtropical subsidence caused by the interaction of the mid-latitude Westerlies and the Asian Monsoon (Rodwell and Hoskins, 1996). Anomalously dry (wet) years are typically related to anomalous high (low) sea level pressure over the North Atlantic (from 45° latitude northward) and the Eastern Mediterranean. These sea level pressure anomalies promote northerly (southerly) winds over Turkey (Eshel and Farrell, 2000). This situation shows a direct linkage between North Atlantic climate variability and hydroclimate shifts in the Eastern Mediterranean (Fig. 1C).

To further elucidate the drivers of Eastern Mediterranean hydroclimate variability on orbital and millennial timescales and its linkage to seasonality changes, we combine new high-resolution paleo-proxy data obtained from a sediment drill core from the closed saline Lake Van (Turkey; Fig. 1D) with a suite of transient earth system model experiments that cover the past 4 glacial cycles.

2. The Lake Van sedimentary record

The lacustrine record of Lake Van (Fig. 1D) was recovered in summer 2010 within the framework of the International Continental Scientific Drilling Program (ICDP) Paleovan project (Litt et al., 2012). Here we present a multi-proxy analysis of high-resolution data of the uppermost 150 mcblf (meter composite below lake floor) of the primary drill site 'Ahlat Ridge' (AR, ICDP Site 5034-2, 38.667°N, 42.669°E, ~360 m water depth, Fig. 1D), which captures variations in lake level, oxygenation, runoff, sediment transport or shoreline distance and vegetation.

2.1. Present-day geography and limnology

Endorheic-basin lakes are particularly well suited for high-resolution paleoenvironmental reconstructions as the volume, the level and the surface area of such lakes are very sensitive to climate variability (evaporation, precipitation, and river inflow), which also
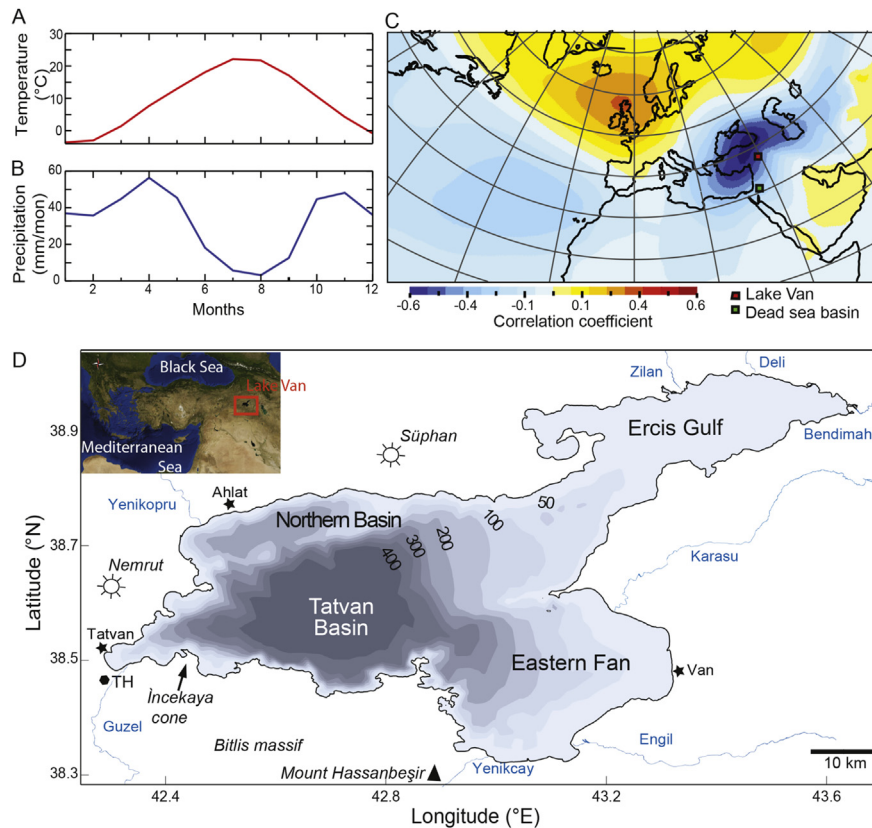
Fig. 1. Modern climatology of the Mediterranean region and map of Lake Van. (A) Temperature climatology from VAN TURKEY (WMO station code 17170) using monthly mean data from 1949 to 2013 (from climexp.knmi.nl); (B) Precipitation climatology from VAN TURKEY (WMO station code 17170) using monthly mean data for 1949—2013 (from climexp.knmi.nl); (C) Correlation between area averaged precipitation minus evaporation anomalies (33—39°E, 38—42°N) and geopotential height anomalies at 850 hPa using data from ERA interim reanalysis (Dee et al., 2011). (D) Bathymetric map of Lake Van (1648 m a.s.l.) with the ICDP PALEOVAN drill sites in the Northern Basin (NB, 5034-1, 38.705°N, 42.567°E) and at Ahlat Ridge (AR, 5034-2, 38.667°N, 42.669°E), showing major lake basins, inflows and cities. The bathymetry of the lake is based on Seyir Hidrografi ve Oşinografi Dairesi, (1990). Two volcanoes (△), Nemrut and Süphan, are adjacent to the lake. A third extinct volcano, the İncekaya hyaloclastite cone, is partly covered by the lake today (Sumita and Schmincke, 2013). The threshold (TH) at 1737 m a.s.l. prevents water from flowing out to the west. The Bitlis massif rises up to 3500 m a.s.l. Süphan and Mt. Hassanbeşir in the Kavuşşahap Mountains rise above 3500 m a.s.l. Additionally, major inflowing rivers and cities (*) are shown.

strongly affects sedimentation processes. Lake Van is situated on a high plateau in eastern Anatolia, Turkey (Fig. 1). The lake is the fourth largest terminal lake and the largest soda lake on Earth (current morphometry: volume: 607 km³, depth: 451 m depth, surface area: 3574 km²). Present lake-level is at an altitude of 1648 m above sea level (a.s.l.). The lake lies within a tectonic depression with a maximum extension of 130 km ENE-WSW (Fig. 1) and has a relatively small catchment area of about 3.55 times the present size of the lake (12.522 km²; Kadioglu et al., 1997). No outlet, high carbonate concentrations, active regional volcanism of Nemrut and Süphan volcanoes (2948 m a.s.l. and 4058 m a.s.l., respectively) as well as subaquatic hydrothermal exhalations are responsible for the high alkalinity (pH 9.7, salinity 21.4‰) of the water (Kaden et al., 2010). The water column undergoes seasonal stratification with epilimnic temperatures reaching up to 25 °C. Annual water mixing during the cold season affects the uppermost 70 m only and thus deep water temperatures are at ~3.3 °C (Stockhecke et al., 2012). A positive net freshwater balance generates a halocline that separates the 'fresh' surface water from the saline deep water and thus reduces deep water exchange (Kaden et al., 2010; Peeters et al., 2000). As mixing is reduced, degrading organic matter continuously consumes oxygen and the oxic—anoxic boundary (OAB) rises in the water column (Stockhecke et al., 2012). The increasing anoxia leads to an enhanced total export and deposition of organic carbon (TOC). As a consequence of an enhanced fresh-water input, the lake level of Lake Van rose by 2 m from 1988 to 1995, deepwater exchange with the surface ceased and thus the mass of the anoxic deep water body grew (Kaden et al., 2010; Stockhecke et al., 2012).

2.2. Lithostratigraphy of the drill cores

The stratigraphic backbone including the detailed lithostratigraphy and the creation of composite section excluding event layers can be found in Stockhecke et al. (2014b). It was shown that the recurrence of similar lithological successions follows the glacial/interglacial cycles since Marine Isotope Stage (MIS) 11. These lithological successions are reflected by variations in total organic carbon (TOC) and calcium carbonate content (CaCO₃). TOC-rich varved (annually-laminated) clayey silts correspond to rising lake levels (in association with a large anoxic deep water body) deposited during the interglacials, TOC-poor banded and mottled clayey silts (in association to an oxygenated hypolimnion) are deposited as consequence of lake-level lowering during the glacials (Stockhecke et al., 2014b). This pattern was confirmed by geological evidence of high and low lake levels (terraces and clinoforms, respectively; Cukur et al., 2014). In order to explore the high frequency (centennial to millennial-scale) variability captured by the lithology we distinguish between varved clayey silt, intercalations of varved clayey silt and frequent turbidites (description and identification of these graded beds see Stockhecke et al., 2014b) and non-varved clayey silt. The intervals of varved sediment furthermore imply pronounced seasonality similar to today (Stockhecke et al., 2012). The intervals of accumulated turbidites are highlighted, however all event deposits were eliminated from the timeseries by the use of the event-corrected depth scale (mcblf-nE, 'meter composite below lake floor no event'; Stockhecke et al., 2014b). Varved (e.g. varved and varved + turbidites) and non-varved periods are used for statistical comparison with seasonal precipitation pattern from model simulations and the precession index.

2.3. Sediment-color data and scanning X-ray fluorescence (XRF)

The surface of the split sediment cores was photographed with a high-resolution line-scan camera installed in Avaatech XRF core scanner at MARUM, University of Bremen. The sediment total reflectance (in a spherical L*A*B* color space with B* denotes a blue-yellow chromaticity) was measured continuously in transects from the high-resolution images with a cross-core length of 2 cm and down-core resolution of 0.03 mm (Fig. S1A). The center of the sediment surface was used and the down-core transects were only shifted to one of the sites to avoid sediment disturbances. The B* reflectance was chosen as it holds highest resolution, highest correlation to the measured TOC contents (correlation coefficient r = 0.6, n = 663) and mimics the NGRIP isotopic stratotype (Andersen et al., 2004). This new high-resolution proxy record is presented as normalized B* reflectance data (Fig. S1A).

The XRF scanner was used to measure the bulk intensities of major elements (e. g., Si, K, Ca) on split core surfaces (Jansen et al., 1998). XRF data were collected every 2 cm down-core over a 1 cm² area with a cross-core slit size of 12 mm using generator settings of 10 kV, a current of 0.2 mA and a sampling time of 10 s. The XRF data was described in Kwiecien et al. (2014), confirming the lithological interpretation of rising lake levels and increasing rainfall during the last four terminations. In this study we combined statistically normalized elemental records of K, Ca, Si on the refined age model (Fig. S1C—E) with the other proxy data B*, TOC and CaCO₃.

2.4. Geochemical and palynological analysis of discrete samples

Discrete samples were taken at a spacing of 2.5 cm over the AR composite record (a total of 1800 samples, Stockhecke et al., 2014b). The freeze-dried and ground sediment samples were analyzed for total carbon (TC; HEKAtech Euro Elemental Analyzer), total inorganic carbon (TIC; Coulometric Inc., 5011 CO₂-Coulometer) and total organic carbon (TOC = TC − TIC). Duplicates of 112 samples yielded standard errors of ±11% for TN, ±3% for TC and ±5% for TIC. TIC weight % of total sediment (wt %) was converted to carbonate wt % by multiplying a stoichiometric factor (8.33) under the assumption that all inorganic carbon is bound as calcium carbonate (CaCO₃). All wt % data are abbreviated to %. Comparison of the CaCO₃ content with the XRF Ca intensity (Fig. S1C) confirm that the lower-resolution quantitative measurements are replicable by the higher-resolution relative changes in XRF Ca intensity as well as by the inverse changes of Si and K reflecting the siliciclastic minerals.

Pollen assemblages of 320 samples were analyzed at 20 cm and 1 m (Litt et al., 2014) sampling resolution for intervals 0—48 and 48—111.5 mblf-nE, respectively. Pollen preparation is described in detail in Litt et al. (2014). For pollen identification the reference collection of the Steinmann Institute (Palaeontology, Bonn) as well as descriptions of the Mediterranean palynoflora were used (Chester and Rains, 2001; Reille, 1990, 1992, 1995, 1998; Van Zeist and Woldring, 1978). The minimum number of terrestrial pollen grains counted in each sample is at least 500. Here, the percentages of deciduous *Quercus* pollen are reported.

2.5. Age model

The age model of the complete sedimentary sequence of Lake Van recovered within the ICDP Paleovan project was presented by Stockhecke et al., 2014a. Various acknowledged dating techniques, such as: absolute and radiometric dating (varve chronology, radiocarbon dating, and argon—argon single-crystal dating) and relative dating (tephrostratigraphy, magnetostratigraphy, ¹⁰Be measurements and climatostratigraphic alignment) techniques were used to construct a robust and precise chronology of the 600,000 year-old Lake Van record (Stockhecke et al., 2014a, Fig. 2). We took advantage of that chronology (gray lines in Fig. 2, Fig. S2) and used it as an initial condition for further refinements by adding three modifications: (i) a slightly refined correlation between Lake
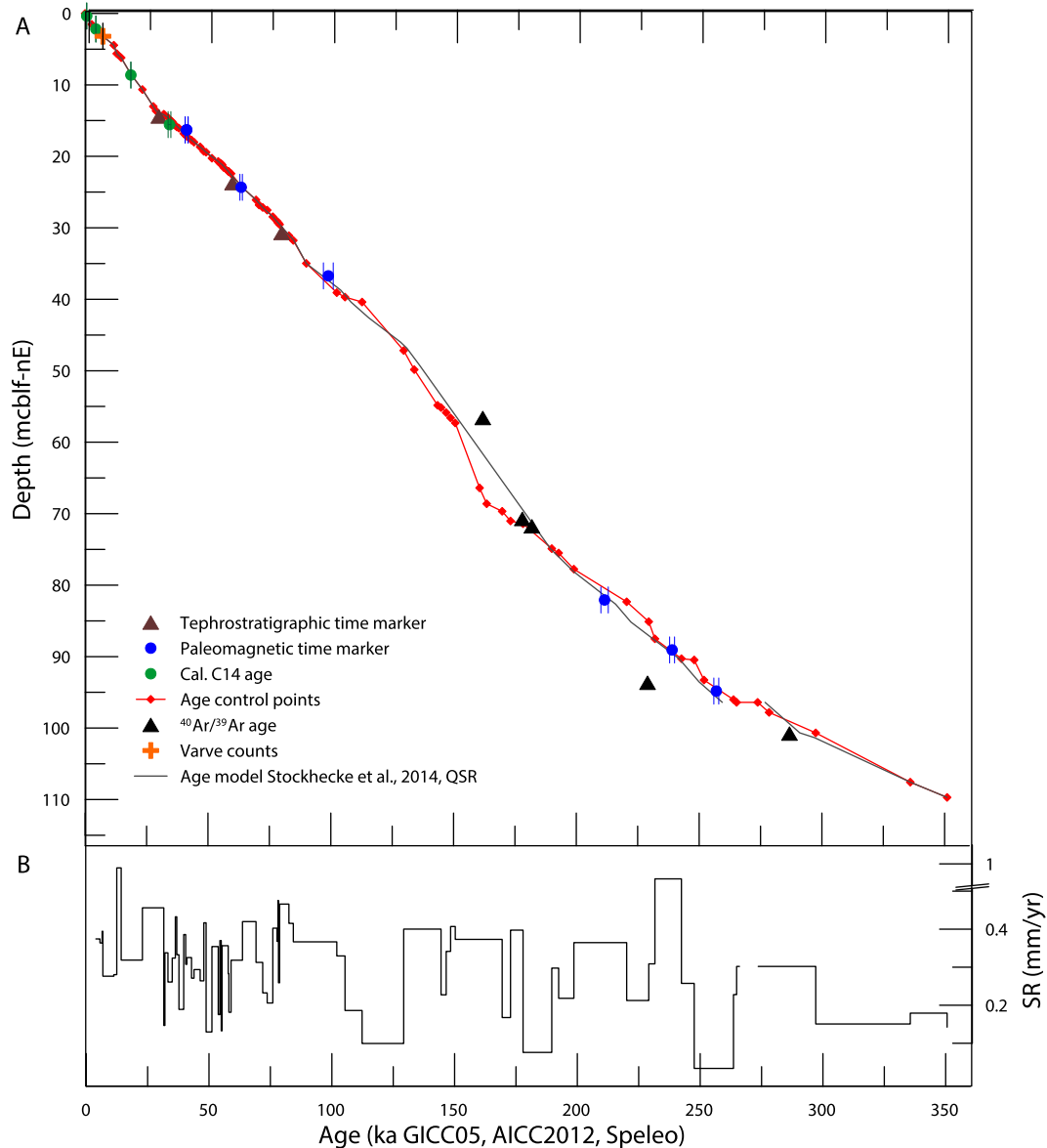
Fig. 2. Chronology of the Lake Van record. (A) Age-depth plot with refined age control points (red), the original chronology (Stockhecke et al., 2014a) and further age constraints from absolute dating and relative ages from other time markers confirming the age model; (B) Sedimentation rates (SR). Gray shaded area represent the interglacials following the Marine Isotope Stage (MIS) boundaries (Lisiecki and Raymo, 2005). (For interpretation of the references to color in this figure legend, the reader is referred to the web version of this article.)

Van B* (sediment) and the δ^{18}O NGRIP record for the time interval (from 0 to 90 kyr) using the GICC05 (Andersen et al., 2004; Rasmussen et al., 2006; Svensson et al., 2008) and GICC05mo-deltext (Wolff et al., 2010) timescales, (ii) integration of the recently published new AICC2012 timescale (Antarctic Ice Core Chronology 2012; Veres et al., 2013) for the time interval from 90 to 125 ka to benefit from the improved dating of Dansgaard-Oeschger (DO) events 23—25 and (iii) correlation of the millennial-scale variability depicted by the high-resolution B* record to the synthetic Greenland record on the Speleo age scale (Barker et al., 2011; Cheng et al., 2009) for the interval beyond 125 ka (Fig. S2).

Our rationale for using different timescales is that the Greenland ice core timescale (for the last 60 ka based on absolute ages by layer counting) and the radiometrically dated speleothem-based timescale are independent of the marine LR04 oxygen isotopic stack (Lisiecki and Raymo, 2005) and orbitally-tuned Antarctica ice-core EPICA Dome C (EDC, Jouzel et al., 2007) timescales, which enables

us to tie the Lake Van record to a global millennial-scale resolved event stratigraphy. The age model details over the full length of the PALEOVAN record including further references are provided in Table S1. Comparison with other timescales shows differences of less than 1—2 kyr (Table S1).

The refined age model consists of 91 age control points (Table S1), which constitute one tie point set to mark the sediment—water interface, five ages from varve chronology and three calibrated 14C ages, 78 tuning-based age control points, and four tie points to set the two gaps and bottom of the record by extrapolation of linear sedimentation rates. The age control points were interpolated using a spline interpolation to avoid abrupt gradient change at each data point, as it would be the case using a linear interpolation.

The comparison of the refined and the original age model reveals that the largest age difference (<10 kyr) occurs during MIS6 (Fig. 2, Fig. S2). This is not surprising as this period was previously

linearly interpolated over 65.5 ka without setting an age control. Additional to the errors, each given in the references of respective timescale (Table S1), we acknowledge that the tuning itself may contain biases that reach up to ~200 years. However, new independent verification of the age model is obtained on orbital time scales through model data correspondence (see below), as well as other relative (magnetostratigraphy, tephrostratigraphy) and absolute (varves counting) and radiometric (argon—argon single-crystal dating) dating methods (Stockhecke et al., 2014a, Fig. 2). Given, these independent constraints, we are confident that the established age model is adequate to study millennial-scale variability and its relation to other paleo-climate records for at least the past 360 ka.

2.6. Statistical analysis of timeseries

The normalized timeseries of the proxy records (Fig. S1) were resampled at 10-year resolution using linear interpolation for further analysis of the joint variability of these records. To extract the common dominant features of multiproxy/temporal variability we conducted an Empirical Orthogonal Function (EOF) analysis of the following variables: B*, Si, K, TOC and Ca. The individual EOF contributions to the overall multiproxy hydroclimate variability can be obtained by multiplying the time-varying principal components (Fig. S3A—C) with their respective EOF pattern values (Fig. S3D—F).

For additional analysis the leading principal component (PC1) was filtered to extract the i) millennial-scale, ii) precessional and iii) lower frequency orbital components. High and low-pass filter with cutoff periods of i) <7 kyr ($PC1_{high}$), ii) >7 kyr ($PC1_{7kyr-low}$), and iii) >35 kyr ($PC1_{35kyr-low}$), were applied.

The high-frequency millennial-scale PC1 ($PC1_{high}$) signal was further subjected to a running variance calculation utilizing a window length of 3 kyr. A bivariate Gaussian kernel density estimator was applied to the combined reconstructed global ice volume timeseries (in meters sea level equivalent, msle; Waelbroeck et al., 2002) and the DO variance (running variance of $PC1_{high}$) to statistically study their relationship.

For statistical pattern analysis and multiple regressions between reconstruction and model data we also applied two band pass filters to PC1 focusing on the obliquity/eccentricity and precession scales using cut-offs at 35—200 and 10—28 kyr, respectively.

3. Climate model experiments

To explore the climate response to changing boundary conditions on millennial and orbital timescales and to compare the Lake Van climate reconstructions with numerical simulations, two transient paleo-climate model experiments were conducted with the LOVECLIM earth system model (Goosse et al., 2010).

3.1. LOVECLIM earth system model

LOVECLIM is a coupled atmosphere-ocean-sea-ice-vegetation model. The atmospheric component ECBilt (Opsteegh et al., 1998) of the coupled model LOVECLIM is a spectral three-level model, based on quasi-geostrophic equations extended by estimates of ageostrophic terms. The model is run in T21 horizontal resolution (~5.6° x 5.6°) and contains a full hydrological cycle which is closed over land by a bucket model for soil moisture and a runoff scheme. The ocean-sea ice component CLIO (Goosse and Fichefet, 1999) is based on a free-surface Ocean General Circulation Model with $3° \times 3°$ horizontal resolution which is coupled to a thermodynamic-dynamic sea ice model. The terrestrial vegetation model "VEgetation COntinuous DEscription" (VECODE; Brovkin et al., 1997) consists of two plant functional types and non-vegetated deserts

zones. Each grid cell assumes a partial coverage by these three land cover types depending on the annual mean temperature and rainfall amount and variability. Vegetation changes feed back to the atmosphere only through corresponding changes in albedo. The effect of evapotranspiration on the atmosphere is not explicitly simulated.

The first LOVECLIM experiment is a global model hindcast from 50 to 11 a (details of the 50—30 ka and 18—11 ka simulations were presented in Menviel et al., 2014 and Menviel et al., 2011 respectively). The second experiment was described in Timmermann et al. (2014) and covers the climate history of the past 408 kyr.

3.2. 50—11 ka global hindcast simulation

Initial conditions for the transient 50—11 ka hindcast simulation were obtained by conducting an equilibrium spin-up simulation using an atmospheric CO_2 content of 207.5 ppmv, orbital forcing for the time 50 ka B.P. and an estimate of the 50 ka B.P. ice sheet orography and albedo which were obtained from a 130 ka off-line ice sheet model simulation (Abe-Ouchi et al., 2007). In the subsequent un-accelerated transient run, greenhouse gases, orbital and ice sheet forcing were updated continuously following the methodology of Timm and Timmermann, 2007 and Timm et al., 2008. Note that our coupled model version used here does not include an interactive ice sheet. Therefore, freshwater release into the ocean as a result of ice sheet calving and ablation are not explicitly captured. To mimic the time-evolution of these terms and their effect on the ocean circulation, we apply an anomalous North Atlantic freshwater forcing to the North Atlantic region 55°W—10°W, 50°N—65°N (Fig. S4B). Negative forcing anomalies can be interpreted as periods of reduced precipitation, calving and runoff into the anomalously saline Arctic Ocean and into Nordic Seas and the absence of Bering Strait Throughflow during the glacial. Positive freshwater anomalies represent times of negative net mass balance of the Northern Hemisphere ice sheet, associated for instance with massive calving events, subsurface melting at the ice-sheet/ice-shelf/ocean interface or surface ablation. The freshwater forcing (FWF) time series is obtained through an iterative procedure (Menviel et al., 2014), that is designed such that the simulated temperature anomalies in the eastern subtropical North Atlantic best match a target alkenone-based sea surface temperature (SST) reconstruction from the Iberian margin core MD01-2443 (Fig. S4D; Martrat et al., 2007). The simulated Iberian margin SST (15°W—8°W, 37°N—43°N) and Atlantic Meridional Ocean Circulation (AMOC) strength (maximum of meridional streamfunction in the North Atlantic) are depicted in Fig. S4D, E.

The model index regions for the paleodata/model comparison are chosen as 41°E—44°E, 37°N—40°N for Turkey rainfall, 15°W—8°W, 37°N—43°N for Iberian margin SST and 38.5°N—44.2°N, 19.7°E—25.2°E for the simulated forest fraction changes in Greece. It should be noted that for model/data comparison the model data were projected onto the GICC05 timescale (see Menviel et al., 2014 for details).

3.3. Transient simulation over the past 408 ka

To study the time-evolving aspects of orbital and greenhouse gas-driven climate changes in the Mediterranean region over the past 408 ka, we also conducted and analyzed a transient LOVECLIM model experiment (Timmermann et al., 2014), which uses time-dependent boundary conditions with an acceleration factor of 5 for orbital parameters (Berger, 1978), CO_2 concentrations, northern hemispheric ice-sheet orography (Ganopolski and Calov, 2011) and albedo over ice sheets, i.e. one coupled model year corresponds to five orbital calendar years. No additional freshwater forcing was
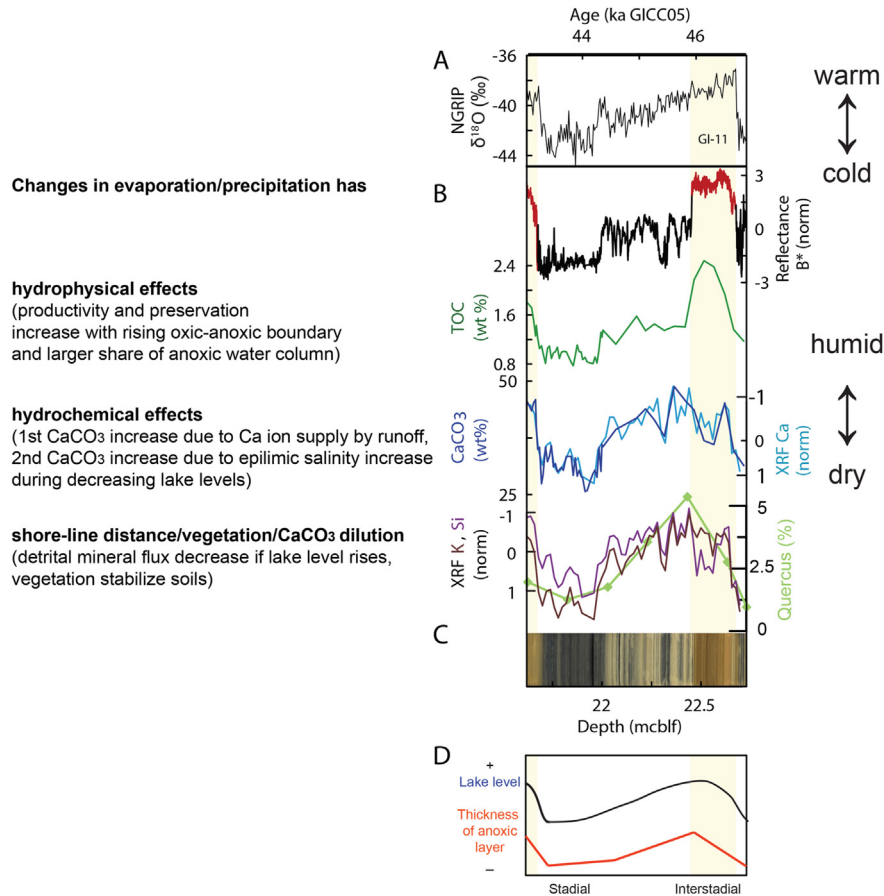
Fig. 3. Schematic of lake dynamics during the transitions from Dansgaard-Oeschger events 11 to 10 (Stockhecke, 2013). (A) NGRIP $\delta^{18}O$ from 43.5 to 46.5 kyr GICC05 (Andersen et al., 2004; Wolff et al., 2010); (B) High-resolution proxy records (B*, TOC, $CaCO_3$, XRF Ca, XRF K and XRF Si intensities) and deciduous *Quercus* pollen percentages on composite depth (21.6–22.75 mcblf); (C) High-resolution line scan image of corresponding sediment surface; (D) Reconstructed lake level variations and changing thickness of the anoxic deep water body.

used to mimic millennial-scale DO variability. The model simulation is compared in detail with the Lake Van hydroclimate data. Furthermore, the simulated precipitation and evaporation data are used to force a simplified lake model for different lake configurations in Turkey and the Levant, mimicking roughly the conditions for Lake Van and Lake Lisan.

3.4. Regression analysis between reconstructed PC1 and model simulations

The normalized hydroclimate PC1 was multiplied with −1 ([PC1*=(−1) (PC1−<PC1>)/(<(PC1−<PC1>)²>)^0.5], where <..> represents the long-term mean value) to determine the typical atmospheric patterns corresponding to the reconstructed drought conditions in the Eastern Mediterranean on millennial, eccentricity and precessional timescales. Positive values of PC1* correspond to drought conditions. For millennial timescales, we just focus on the period 50–30 ka and use an unfiltered reconstructed PC1*. For the eccentricity (precession) timescales, we used the 35–200 kyr bandpass filter to PC1*, respective 10–28 kyr for precession scales. PC1* for the respective timescales is then regressed onto the LOVECLIM simulated anomalies of 800 hPa geopotential height anomalies and relative rainfall changes from the 408 ka transient experiment (for eccentricity and precession timescales; Timmermann et al., 2014) and the DO hindcast simulation (for millennial timescales; Menviel et al., 2014).

4. Lake-level simulations

We develop a simplified lake level model for two different regions (Turkey and Levant) that is driven by local precipitation (P_m), and evaporation (E_m) output from the 408 ka transient LOVECLIM simulation. The model index regions for the lake level models are chosen as 41°E–44°E, 37°N–40°N for simulation of Lake Van levels and 30°N–33°N for simulation of Lake Lisan levels and we focus on the last 85 ka and orbital timescales only. For the Lake Lisan model, the LOVECLIM model timeseries for precipitation (P_m) and evaporation (E_m) were bias corrected with

$$E*(t) = [E_m(t) - E_m(t = 0 \text{ ka})] + E_{obs} \quad (1)$$

$$P(t)* = \beta[P_m(t) - P_m(t = 0 \text{ ka})] + P_{obs} \quad (2)$$

such as to match approximately the modern mean Dead Sea evaporation rates $E_{obs} = 110$ cm/year and the mean precipitation over the catchment area of $P_{obs} = 10$ cm/yr, similar to the values used in ref. Rohling (2013). Taking into account the effective ratio between catchment area and lake surface area (γ), we further assume that the long-term mean freshwater balance is zero.

$$\langle \gamma \cdot P* - E* \rangle = 0 \quad (3)$$

where $\langle \gamma \cdot P* - E* \rangle$ denotes the mean from 0 to −85 ka. This balance Equation (3) together with Equations (1) and (2) allow us to determine the precipitation scaling factor β in Equation (2). To
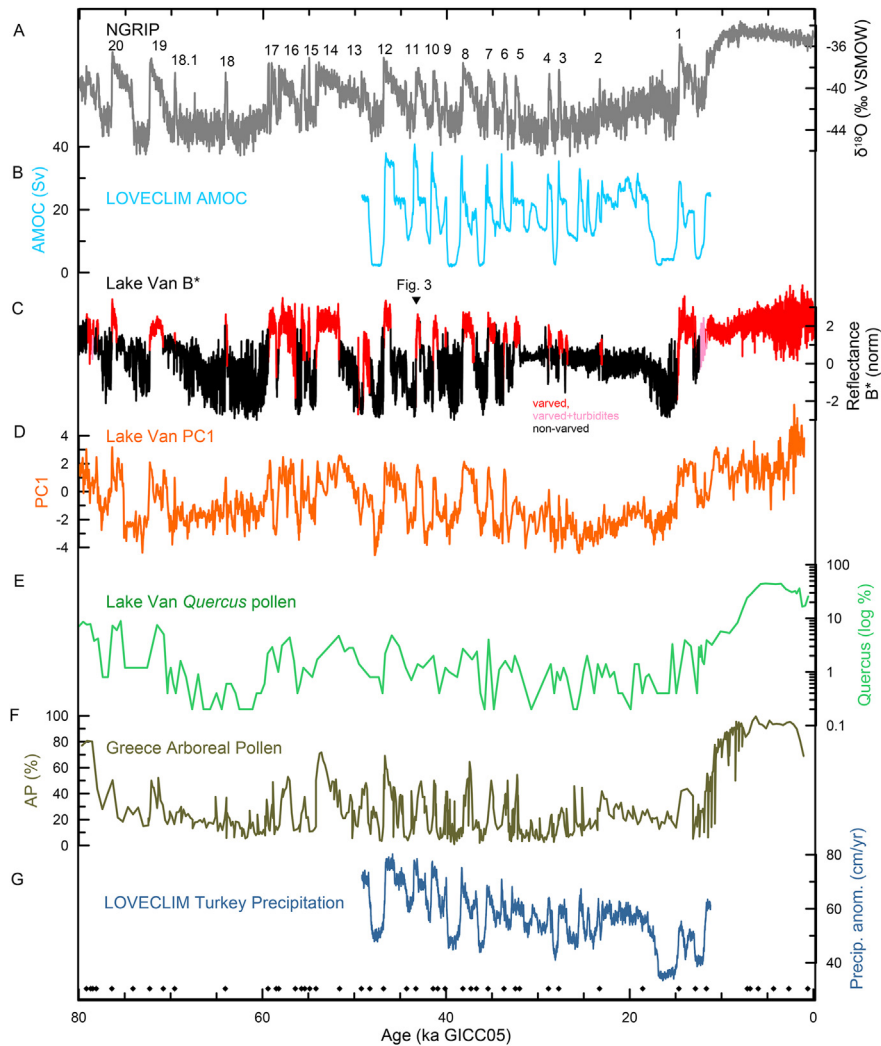
Fig. 4. Paleoreconstruction and model comparison for Dansgaard-Oeschger events from 0 to 80 kyr. (A) NGRIP δ^{18}O (Svensson et al., 2008); (B) Simulated maximum of the North Atlantic meridional streamfunction [1 Sv = 10^6 m^3/s] representing the Atlantic Meridional Overturning Circulation (AMOC) in LOVECLIM (Menviel et al., 2014); (C) Lake Van B* reflectance color record; (D) Lake Van PC1 hydroclimate record; (E) deciduous *Quercus* pollen percentage (on logarithmic ordinate) from Lake Van; (F) Arboreal pollen from Tenaghi Philippon, Greece (Muller et al., 2011) synchronized to the NGRIP; (G) Simulated LOVECLIM precipitation changes over Turkey. Black diamonds depict the age control points. (For interpretation of the references to color in this figure legend, the reader is referred to the web version of this article.)

obtain estimates for the evolution of the anomalous Lake Lisan level we integrate the freshwater balance in time L(t) = $\int_{t=85ka}$ dt [γ P*(t) − E*(t)]. Representing the fact that a considerable fraction of rainfall in the catchment area of Lake Lisan, which was about 40 times larger (Rohling, 2013) than the current size of the Dead sea, is lost through evaporation, we choose an idealized, yet representative, value of γ = 9.8. A similar approach is pursued for Lake Van, using γ = 3.55 (see Section 2.1) and P$_{obs}$ = 37 cm (Fig. 1) and E$_{obs}$ = 110 cm/yr, similar to the values used in Lemcke (1996). The idealized lake model experiments discussed here should be considered possible scenarios, which are based on reasonable assumptions, not as an exact reproduction of the real lake level trajectory over the last glacial cycle.

5. Results and discussion

5.1. Hydroclimate timeseries from Lake Van

Extending back to 600 ka (of the sedimentStockhecke et al., 2014b), the partly-varved sedimentary section of Lake Van allows for an unprecedented view into the millennial to orbital-scale

modulation of subtropical hydroclimate changes and its relation to North Atlantic climate change and external forcing. Rising conditions of Lake Van water levels, associated for instance with increased precipitation (or reduced evaporation), typically lead to both a reduction of surface salinity and deep lake mixing, which resulted in an expansion of the volume of the anoxic deep water body (Kaden et al., 2010). Such conditions caused the enhancement of net export, deposition and preservation of organic carbon (Stockhecke et al., 2014b). These hydroclimate changes are well documented by shifts in sediment colorof the sediment(B*; Fig. 3B). Furthermore, pluvials can lead to an increase in the terrestrial sediment transport distance between the coring site and the lake shore-line as well as to an increase in calcium ion supply. Both of these factors resulted in a reduction of the silici-clastic minerals and in an increase of autochthonous carbonate and subsequent relative shifts in the composition of the sediments. Thus, complementary information on hydroclimate changes in the Lake Van region can be derived from other sedimentary data such as total organic carbon (TOC), calcium carbonate (CaCO$_3$, Ca), silica (Si) from quartz, feldspar, clay minerals and potassium (K) from latter two (Fig. S1C to E).

The high-resolution B* sediment color record (Figs. 3B and 4C) is correlated with Greenland oxygen-isotope variations (Andersen et al., 2004, Figs. 3A and 4A) and North Atlantic temperature anomalies (Fig. 5B) of DO variability during MIS 5-2. It captures millennial-scale variability during glacial periods for the past 360 kyr.

Applying an Empirical Orthogonal Function (EOF) analysis to the timeseries of B*, Si, K, TOC and Ca (all sensitive to hydroclimate variations in the Lake Van region) helps us to extract the common features of multiproxy/temporal hydroclimate variability (see Section 2.6).

The explained variances for each EOF mode attain values of 56% (EOF1), 28% (EOF2) and 9% (EOF3). Positive values of the leading principal component (PC1) are associated with high B* (anoxic conditions, intensified stratification), anomalously low Si and K (increased shore-line distance, increased runoff and forested vegetation in watershed), positive TOC contents (anoxic conditions, intensified stratification and productivity) and positive $CaCO_3$ anomalies (increased supply via runoff of Ca^{2+} ion into lake). PC1 (Figs. 4D and 5D) captures both orbital-scale variability and millennial-scale flickering of hydroclimate conditions in the Eastern Mediterranean associated with DO variability.

### 5.2. Millennial-scale climate variability

5.2.1. Comparison of Lake Van hydroclimate reconstruction with DO hindcast simulation

To explore the underlying dynamics of DO-related Eastern Mediterranean hydroclimate variability from 50 to 11 ka (Fig. 4), we compare the reconstructed changes in B* and PC1 with rainfall changes simulated by the transient DO LOVECLIM hindcast experiment (Menviel et al., 2014) described in Section 3.2. In response to the applied anomalous North Atlantic freshwater forcing (Fig. S4A), the model simulates a weaker Atlantic Meridional Overturning Circulation (AMOC) during DO and Heinrich stadials (Fig. 4B), cooling of the North Atlantic in accordance with Iberian margin SST reconstructions (Martrat et al., 2007; Fig. S4C, D) and extended droughts in the Eastern Mediterranean (Fig. 4G), in agreement with the Lake Van B* and PC1 records and deciduous *Quercus* pollen percentages (Fig. 4C to E). This close qualitative correspondence between AMOC changes and Eastern Mediterranean droughts is further supported by arboreal pollen percentages from Tenaghi Philippon, Greece (Tzedakis et al., 2006, Fig. 4F), which show massive retreat of temperate forest during stadial periods and an increase to about 40—60% during interstadials.
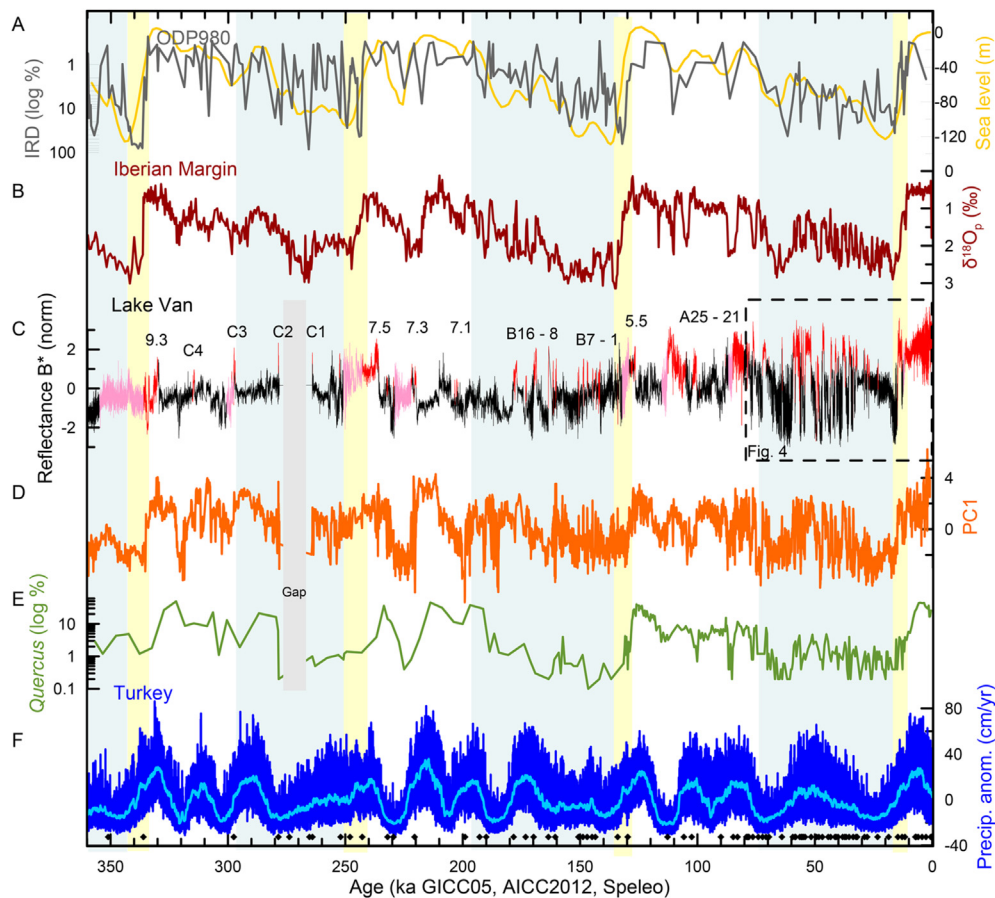
Fig. 5. North Atlantic and Mediterranean climate variability from 0 to 360 ka. (A) Percentage of ice-rafted debris (IRD on Speleo timescale, in gray) from core North Atlantic core ODP980 (McManus et al., 1999) on logarithmic ordinate and reconstructed sea level data (on its original timescale, in yellow; Waelbroeck et al., 2002); (B) $\delta^{18}O$ of planktic foraminifera from Iberian Margin core (on Speleo timescale; Hodell et al., 2013); (C) Lake Van B* reflectance color record; (D) Lake Van PC1 hydroclimate record; (E) deciduous *Quercus* pollen percentage from Lake Van (on logarithmic ordinate) from Lake Van; (F) Simulated annual mean precipitation anomalies (dark blue; averaged over 41—44°E, 37—40°N) from a transient earth system model simulation conducted with LOVECLIM and 500-yr running mean (light blue; Timmermann et al., 2014). Black diamonds depict the age control points. Shaded area represents the gap (gray), the glacials (blue) and the terminations (yellow) following the Marine Isotope Stage (MIS) boundaries (Lisiecki and Raymo, 2005). Interglacial substages follow the nomenclature of Jouzel et al., 2007. Dansgaard-Oeschger events of the last glacial (A1-25, see Table S1 for references), of MIS 6 (B16-1) and of MIS 8 (C4—C1) are enumerated continuously. (For interpretation of the references to color in this figure legend, the reader is referred to the web version of this article.)
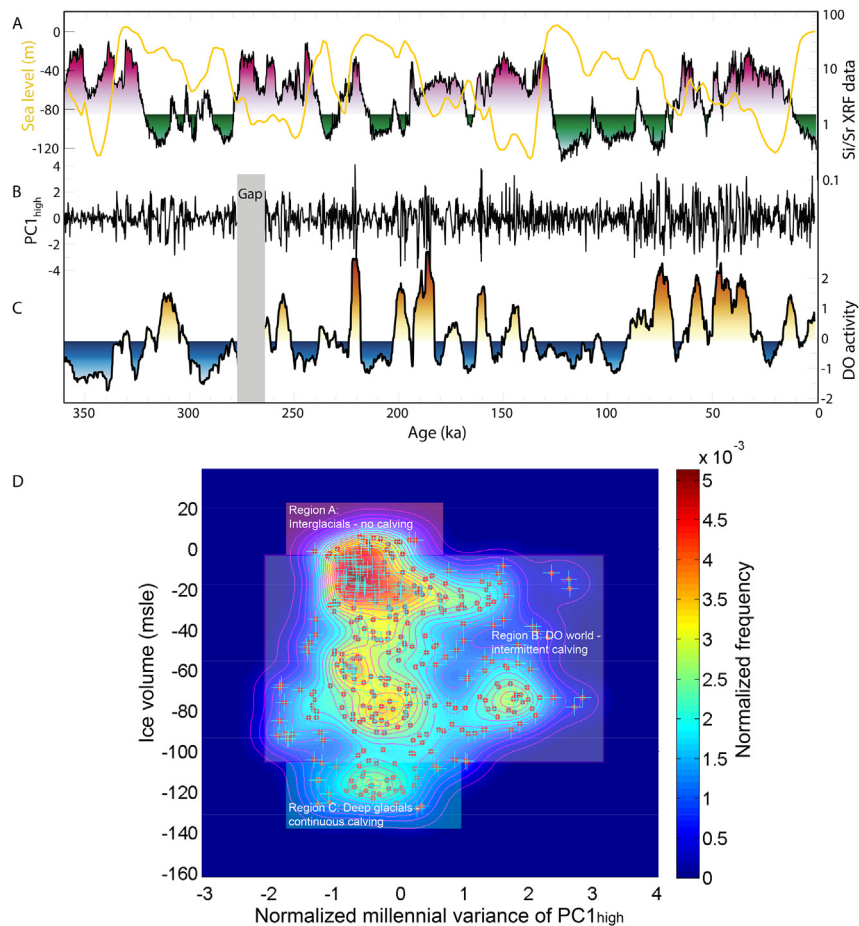
Fig. 6. Orbital-scale modulation of Dansgaard-Oeschger variance. (A) Si/Sr XRF data (black line) from North Atlantic site U1308 (Hodell et al., 2008) on logarithmic ordinates, as a proxy for silicate-rich ice-rafted debris and sea level reconstruction (Waelbroeck et al., 2002; yellow); (B) High-frequency contribution of Lake Van hydroclimate PC1 (PC1high); (C) Normalized running standard variance of PC1high. (D) Normalized millennial variance of PC1high compared with the global ice volume (in meters sea level equivalent, msle) in a two-dimensional histogram. Region A reflects the interglacial periods of low ice volume and no calving events, region B reflects the periods of intermediate ice volume and intermittent calving events, region C marks the periods of high global ice volume during the glacials associated with continuous calving. (For interpretation of the references to color in this figure legend, the reader is referred to the web version of this article.)

5.2.2. Modulation of DO variability by ice volume

DO variability in the high-resolution Lake Van hydroclimate records can be traced back far beyond the last glacial period. The DO variance timeseries from $PC1_{high}$ shows several episodes of DO bursting within glacial periods (Fig. 6C), such as from 140 to 160 ka, 184–205 ka, 220–237 ka, 250–263 ka and 307–321 ka in alignment with periods of high IRD in the North Atlantic (Fig. 6A) representing unstable ice-sheets. The comparison between the variance changes of the high-pass PC1 and of a synthetic record of millennial-scale bipolar seesaw activity (Barker et al., 2011; Fig. S2) reveals a very good agreement until 220 ka, but insignificant correlations prior to that time. We conclude that at least until MIS7, the Lake Van hydroclimate record accurately tracks the timing of ice-sheet induced changes in the strength of the AMOC and the continuum of DO and Heinrich variability in the North Atlantic. More high-resolution and well-dated records of DO variability from MIS8 and beyond are needed to further establish the exact timing of the DO bursting periods and their individual DO events.

Quantification of the relationship between reconstructed global ice volume (in meters sea level equivalent, msle; Waelbroeck et al., 2002) and DO variance (normalized high-frequency PC1) using a bivariate Gaussian kernel density estimator documents that neither interglacials (Fig. 6D, region A), nor deep glacial periods (Fig. 6D, region C) support high levels of millennial-scale variability. Within the window corresponding to ~20–100 m sea-level drops (Fig. 6D,

region B), higher millennial-scale DO variance resulted from intermittent ice-sheet calving and associated AMOC fluctuations. If ice-sheets were small, they took a long time to reach the ocean and build up instabilities that were large enough to generate freshwater and iceberg surges, which affected the AMOC and hydroclimate in the remote Eastern Mediterranean. Thus, during MIS5, interstadials were very long relative to the stadial periods. For very large ice-sheets, negative mass balance terms were much larger and background calving and ablation caused lower North Atlantic sea surface salinities, which lead to a longterm moderate weakening of the AMOC and enhanced drought in the Eastern Mediterranean. In this scenario, MIS2 can be viewed as a near-continuous DO stadial, which was further amplified by additional freshwater discharge during Heinrich event 2 around 24 ka and additional orbital-scale effects.

5.3. Orbital-scale climate variability and seasonality

The Lake Van PC1 hydroclimate record and deciduous *Quercus* percentages (Fig. 5D, E) exhibit pronounced variability on orbital timescales i.e., on precession, obliquity and eccentricity timescales (Fig. 7). To further elucidate the underlying mechanism for the orbital modulation of drought intensities in the Eastern Mediterranean we compare the Lake Van record with the transient LOVECLIM earth system model experiment that covers the past 408 ka (Timmermann et al., 2014) and simulates the global climate
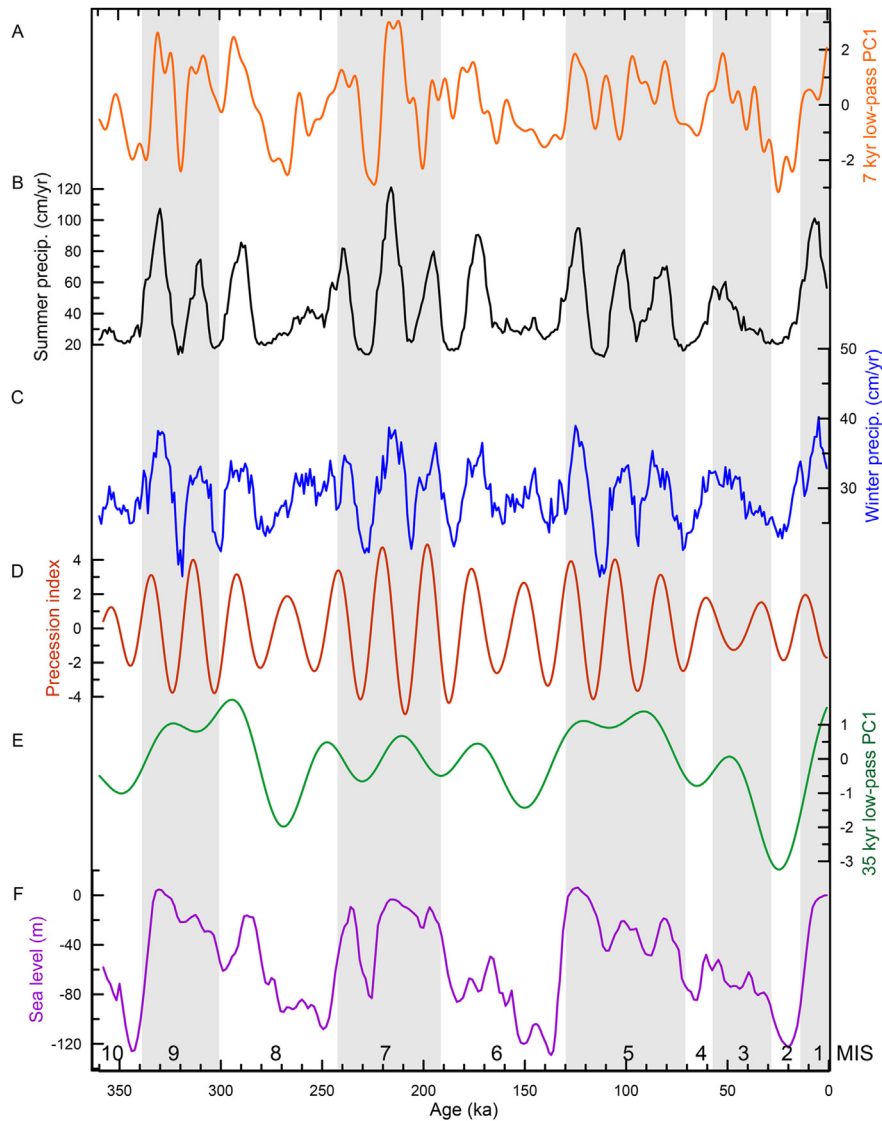
Fig. 7. Lake Van hydroclimate orbital variability compared with model precipitation, external forcing and sea level changes. (A) 7 kyr low-pass filtered PC1 (PC1$_{7kyr-low}$); (B) Simulated summer (JJA) precipitation (on model timescale); (C) Simulated winter (DJF) precipitation (on model timescale); (D) Precession index; (E) 35 kyr low-pass filtered PC1 (PC1$_{35kyr-low}$) and (F) sea level (Waelbroeck et al., 2002). Summer or winter precipitation changes could have caused changes in the precession cycle which affected the PC1. Gray shaded area represent the interglacials following the Marine Isotope Stage (MIS) boundaries (Lisiecki and Raymo, 2005).

response to orbital, ice sheet and greenhouse gas forcing (see Section 3.3). The simulated mean annual rainfall changes over Turkey agree qualitatively well with orbital-scale variability of PC1 (Fig. 5D, F).

To better illustrate the effect of orbital forcings on seasonality changes in precipitation, we calculated the percentage of monthly rainfall for each year relative to the annual mean for this year (Fig. 8E). Under various climate conditions the LOVECLIM model simulates a semi-annual cycle in rainfall with peak rainfall in May and October (Fig. 8F), in good agreement with present-day observations (Fig. 1). Compared to the observations, however, the simulated late fall/early winter peak is somewhat underestimated. The Hovmoller diagram in Fig. 8D documents orbital-scale shifts in the seasonality of the simulated rainfall relative to the annual mean for each year. The largest orbital-scale changes in seasonal rainfall occur in boreal summer, when drought conditions alternate on precessional and eccentricity timescales with wet conditions (15% of the annual precipitation falling in June). These variations are also reflected in Fig. 7, which shows a near quadrupling of simulated summer precipitation rates between

extreme orbital/ice-volume conditions. Furthermore, we used sections of the Lake Van core, where laminations are present and respectively absent and calculated a composite seasonal cycle for these times of rainfall using the LOVECLIM climate model data and a composite normalized frequency distribution of the precession index (Fig. 8F). We can clearly see that periods of lamination in the Lake Van record corresponds an enhanced seasonal cycle of simulated rainfall and a stronger precession index (boreal summer in perihelion).

Under current conditions a hot and dry summer season separates the two seasonal precipitation maxima in April and in October/November (Fig. 1A, B). According to the transient model simulation (Fig. 8D, E) and previous studies (Kutzbach et al., 2014), periods with maximum seasonality in boreal insolation (positive precession index) caused an increase of both spring to summer rainfall (Fig. 8E) and storm track-driven winter precipitation (Fig. 7C). This process in turn affected the amplitude of precipitation seasonality, the mean annual rainfall and runoff into Lake Van, as documented by the correspondence between periods of varved
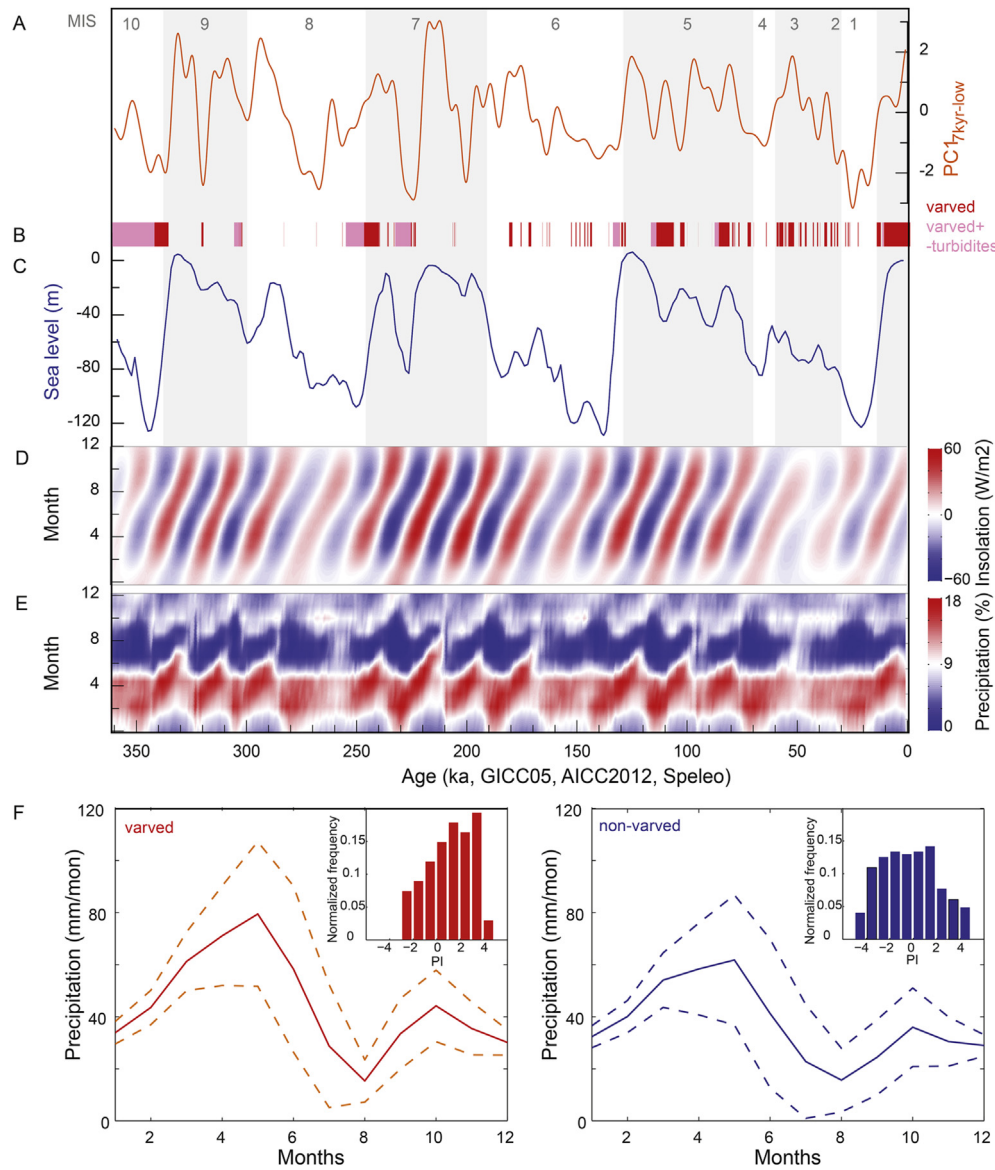
Fig. 8. Ice sheet and orbital effects on hydroclimate in Turkey from 0 to 360 ka. (A) Low-pass filtered PC1 (PC1$_{7kyr-low}$); (B) Periods of lamination in Lake Van (red: varved, pink: varved and turbidites, white: non-varved); (C) Reconstructed global sea level changes (on its original timescale; Waelbroeck et al., 2002); (D) Hovmoller diagram of monthly insolation changes at Lake Van latitude; (E) Hovmoller diagram of simulated monthly precipitation changes (averaged over 41–44°E, 37–40°N) over Turkey relative to the annual mean of any given year. Gray shaded area represent the interglacials following the Marine Isotope Stage (MIS) boundaries (Lisiecki and Raymo, 2005); (F) Normalized frequency distribution of simulated rainfall in Lake Van region for varved intervals (red, left) and for non-varved intervals (blue, right) according to the lithostratigraphy of the record (Stockhecke et al., 2014b) with inlets of normalized frequency distribution for precession index (PI). (For interpretation of the references to color in this figure legend, the reader is referred to the web version of this article.)

sediment (Fig. 8B), enhanced seasonal forcing and increased simulated rainfall seasonality (Fig. 8F).

5.4. Large-scale hydroclimate patterns

Multiple regressions between the Lake Van hydroclimate PC1 and the LOVECLIM model simulation were conducted to determine the typical atmospheric patterns corresponding to the reconstructed drought conditions in the Eastern Mediterranean on millennial, eccentricity and precessional timescales. This analysis searches for the large-scale simulated circulation patterns that correlate closely with reconstructed hydroclimate changes in Lake Van. The results are shown in Fig. 9 and have been schematized for Fig. 10. We find that on all timescales, droughts in the Eastern Mediterranean are a large-scale phenomenon,

associated with stronger mean annual anticyclonic circulation and increased atmospheric subsidence (not shown here) in the Eastern Mediterranean and typically cold surface conditions in the North Atlantic. A reconstruction of the associated atmospheric circulation pattern reveals that precessional-scale hydroclimate anomalies in Lake Van PC1 were part of a large-scale hydroclimatic pattern extending across the Eastern Mediterranean, North Africa and the Middle East (Figs. 9C and 10D depicting drought conditions).

A significant portion of eccentricity-scale (100–120 kyr) variability can also be seen in PC1 and the simulated rainfall changes (Fig. 8). Interglacials in Turkey were relative wet (positive PC1 loading) and glacials were relatively dry (negative PC1 values), in accordance with lake-level reconstructions (Cukur et al., 2014; Kuzucuoglu et al., 2010; Stockhecke et al., 2014b)
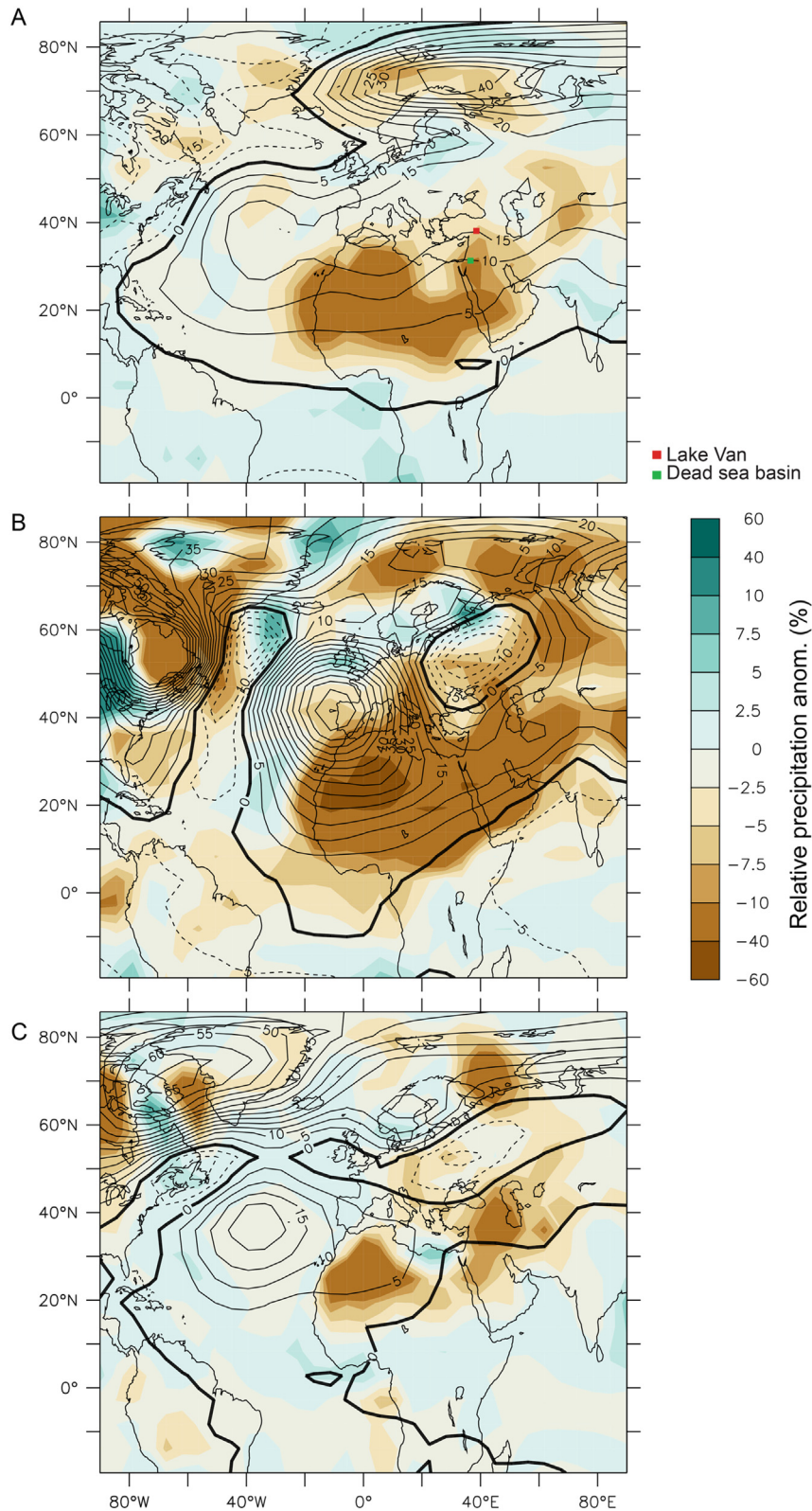
Fig. 9. Relationship between reconstructed droughts and simulated climate data on millennial, eccentricity and precession timescales. (A) Model/paleodata regressions between simulated 800 hPa geopotential height changes (contour, m²/s²), relative precipitation changes (%) and negative normalized Lake Van PC1 (Fig. 1) from 50 to 30 ka, capturing the key pattern of DO stadials; (B) same as (A), but using reconstructed negative normalized band-pass filtered (35–200 kyr) PC1 from Lake Van (Fig. 7), capturing the ice sheet effects; (C) same as (A), but using reconstructed negative normalized band-pass filtered (10–28 kyr) PC1 from Lake Van, corresponding to negative precession index values and minimum insolation seasonality (Fig. 7).
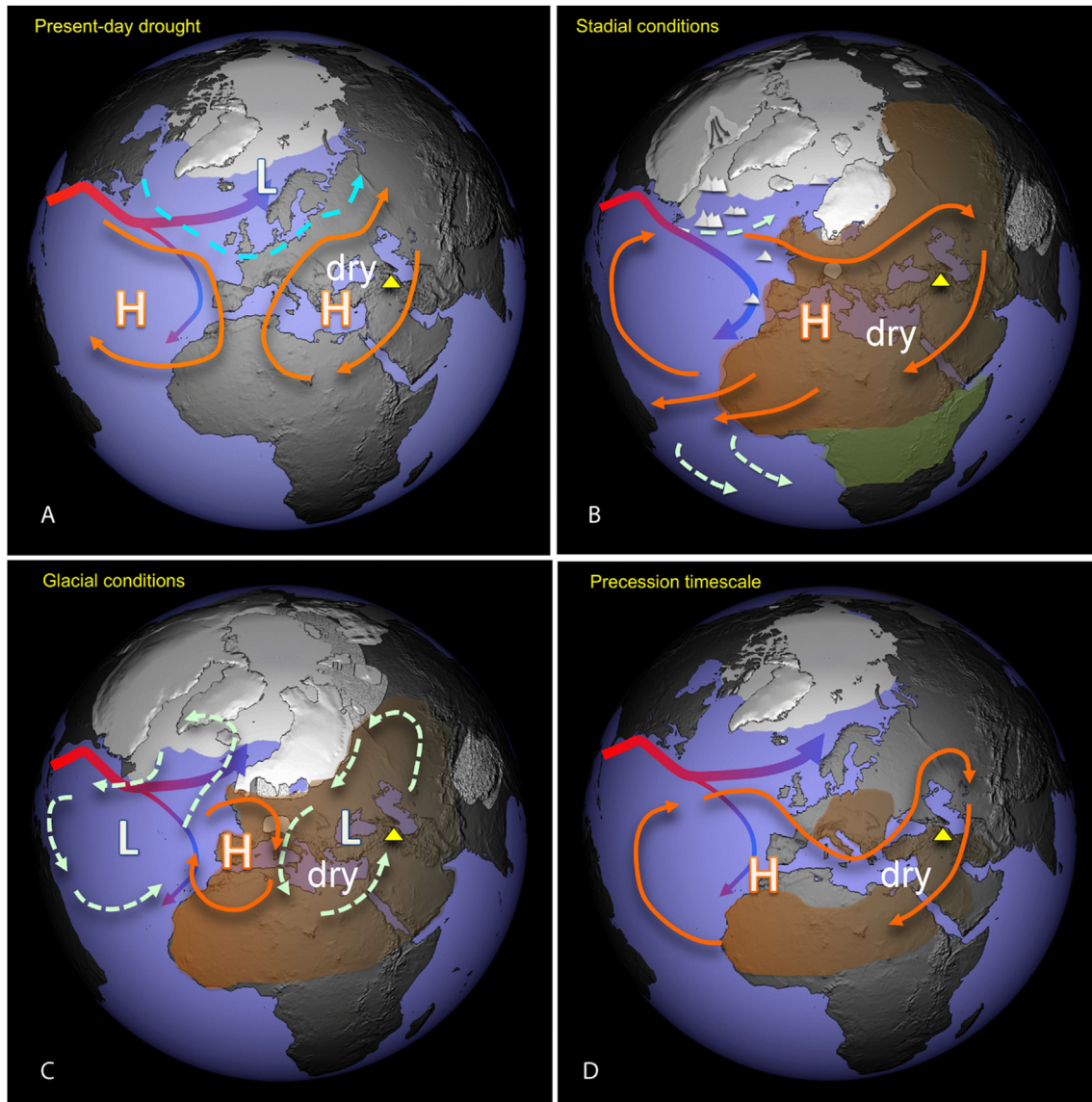
Fig. 10. Schematic pattern of sea-level pressure, wind (cyan/orange contours), precipitation (green/brown shading) anomalies and ocean currents (red-blue arrow) for Eastern Mediterranean droughts occurring for present day conditions (A), on millennial (B; DO stadials), eccentricity (C; glacial periods) and precessional timescales (D, negative precession index). The schematic is based on the analysis in Figs. 1 (for A) and 9 (for B to D). Yellow triangle marks Lake Van. (For interpretation of the references to color in this figure legend, the reader is referred to the web version of this article.)

and the deciduous *Quercus* pollen percentages (Litt et al., 2014) from Lake Van, which show advances and retreats of the oak steppe-forest, respectively (Fig. 5E). This variability results from the ice-sheet orographic forcing (Fig. 7E, F), the associated anomalous atmospheric subsidence (Timm et al., 2010) and shifts in atmospheric pressure patterns (Figs. 9B and 10C). The ice-sheet effects from both the Laurentide and the Eurasian ice sheets caused massive drying over the Mediterranean and Northern Africa (Fig. 10C).

5.5. Glacial droughts and lake levels in the Levant region

The evidence presented here (Figs. 4, 5 and 8) for reduced glacial rainfall in eastern Turkey is consistent with the larger-scale pattern of dry glacial and humid interglacial conditions reconstructed from lakes, speleothems and peat bogs in the Mediterranean and northern Levant (Lago Grande di Monticchio (Allen et al., 2000); Lake Ohrid (Vogel et al., 2010); Ioannina (Tzedakis, 1994); Tenaghi

Philippon (Fletcher et al., 2013; Tzedakis et al., 2006); Sofular Cave (Fleitmann et al., 2009); Karaca Cave (Rowe et al., 2012); Lake Urmia (Stevens et al., 2012); Lake Yammoûneh (Gasse et al., 2015 and references therein; Fig. 11)). Furthermore our data lend support to previous interpretations of speleothem data from the central Levant region (Bar-Matthews et al., 2003). Speleothems from the southern Negev deserts (Vaks et al., 2010) and dated lake deposits from the Nafud desert (Rosenberg et al., 2013) indicate interglacial pluvial periods synchronous with sapropel layers in the Mediterranean (Zhao et al., 2011). These findings have been linked to an intensification of the Atlantic-Mediterranean cyclone activity and an enhancement of monsoon-like rain.

However, the evidence for large-scale glacial drying in the Eastern Mediterranean and Levant region, appears to be at odds with the evidence for high (low) glacial (interglacial) lake stands of lacustrine bodies which evolved within Dead Sea basin (DSB; central Levant, 400 m b.s.l.), such as the mid-Pleistocene Lake Amora, the late Pleistocene Lake Samra, the last glacial Lake Lisan
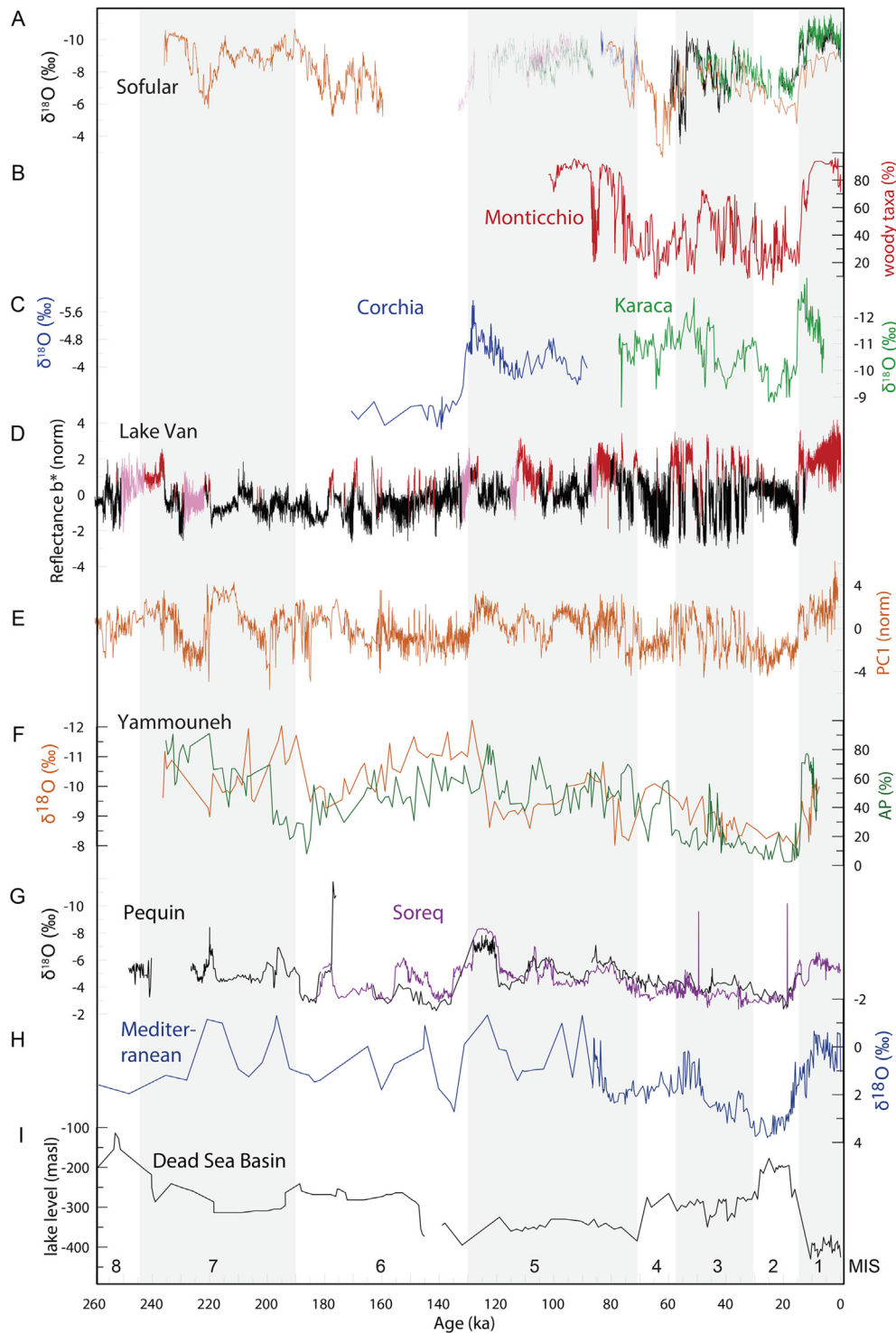
Fig. 11. Comparison of different paleo-archives over 260 ka from the Mediterranean and the Levant. (A) δ¹⁸O from the Sofular cave (Badertscher et al., 2011); (B) Woody taxa from the Lago Grande di Monticchio (Allen et al., 1999); (C) δ¹⁸O from the Karaca cave (Rowe et al., 2012) and δ¹⁸O from the Corchia cave (Drysdale et al., 2005); (D) Lake Van B* (this study); (E) Hydroclimate PC1 (this study); (F) δ¹⁸O and Arboreal pollen (AP) from the Lake Yammoûneh (Develle et al., 2011; Gasse et al., 2015); (G) δ¹⁸O from the Soreq and Peqiin caves (Bar-Matthews et al., 2003); (H) δ¹⁸O from the Eastern Mediterranean Sea (Almogi-Labin et al., 2009; Kroon et al., 1998); (I) lake levels of the Dead Sea Basin (DSB) lacustrine bodies (Waldmann et al., 2009; Waldmann et al., 2010). All data are shown on it original timescales. Gray shaded area represent the interglacials following the Marine Isotope Stage (MIS) boundaries (Lisiecki and Raymo, 2005).

(~70–14 kyr), and the Holocene Dead Sea (Torfstein et al., 2015; and references therein) as well as with the increased growth of speleothems under glacial conditions (Frumkin et al., 2011). The anomalous lake stands and speleothem growth periods have been interpreted in terms of increased (decreased) glacial (interglacial)

rainfall (Enzel et al., 2008). While lake levels variations of the DSB lakes contrasts regional reconstructions on orbital timescales, are they in line with other regional reconstructions on millennial timescales, e.g. rise during interstadials (including MIS5.5, 5.3, 5.1) and fall during stadials (including MIS5.4 and 5.2). In particular,
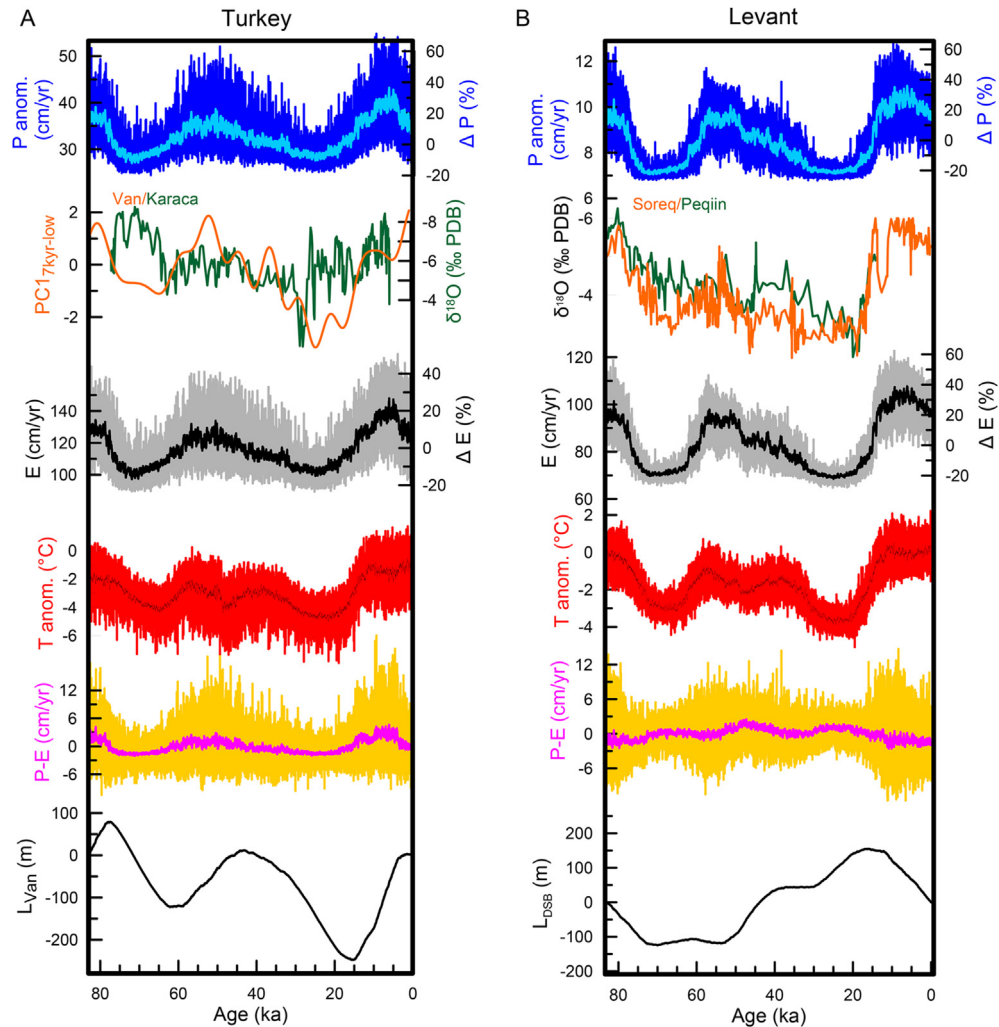
Fig. 12. Lake level experiment for Eastern Turkey (A) and the Levant (B) from 0 to 80 kyr. From top to bottom: (A) Timeseries of precipitation anomalies over Turkey (P anom.), low-pass PC1 and speleothem δ18O record from Karaca (eastern Turkey; Rowe et al., 2012), evaporation (E), temperature anomaly (T anom.), precipitation–evaporation (P–E) and time-integrated lake level (L_Van); (B) Timeseries of precipitation anomalies over Levant (P anom.), speleothem δ18O record from Soreq and Peqiin cave in Israel (400 m respective 650 m a.s.l.; Bar-Matthews et al., 2003), evaporation (E), temperature anomaly (°C, T anom.), precipitation–evaporation (P–E) and time-integrated lake level (L_DSB). The running means (31-point moving window) are overlain and the second ordinates reflect the relative change of the anomalies in P and E at each site.

Heinrich stadials are reflected by Gypsum units in the Lisan formation, which were formed during lake-level decreases and water column mixing (Stein et al., 1997; Torfstein et al., 2015, 2009, Neugebauer et al., 2014). Numerous studies have tried to explain or reconcile this conundrum (Enzel et al., 2008; Frumkin et al., 2011; Kutzbach et al., 2014; Rohling, 2013; Stein et al., 2010; Torfstein et al., 2013; Tzedakis, 2007), which is apparent on orbital, but not on millennial timescales related to Dansgaard-Oeschger and Heinrich variability (Bartov et al., 2003).[1]

To reconcile the interpretations of Lake Van hydroclimate and

Lake Lisan level data in terms of the large-scale hydroclimate patterns identified in Figs. 9 and 10 we present a simple numerical model that is driven by the simulated LOVECLIM precipitation and evaporation changes in these regions. We suggest, that the relative glacial changes in precipitation may have been smaller than those for evaporation in DSB, thus leaving a delicate, but positive freshwater balance for Lake Lisan, even though precipitation was also reduced in glacial times. We would like to stress that according to our model simulation precipitation was reduced in both localities, but clearly not completely absent. We thus suggest that a longterm reduction in precipitation does not rule out the possibility that Lake Lisan experienced occasional "freshening" and supply of bicarbonate and sulfide via runoff or subsurface saline aquifers (Lazar et al., 2014) or via freshwater (Neugebauer et al., 2014, Stein et al., 1997; Torfstein et al., 2015, 2009). This would help explain the aragonite precipitation and gypsum deposition (Stein et al., 1997). However, the possibility of a positive water balance is illustrated by using precipitation and evaporation data (P_m, E_m) for the DSB region from our 408 ka climate model simulation as forcings for our highly idealized lake level model. Note, that this model

---

[1] It should be noted that the interpretation of speleothem growth for only wet periods is quite controversial, because as a result of changing infiltration co-efficients, less precipitation is required for speleothem growth in cold climates Bonacci, O., 2001, Analysis of the maximum discharge of karst springs. Hydrogeology Journal, 9(4): 328–338. Furthermore, changes in relative humidity may have also contributed to increased speleothem growth during glacials Frumkin, A., Bar-Yosef, O. and Schwarcz, H.P., 2011, Possible paleohydrologic and paleoclimatic effects on hominin migration and occupation of the Levantine Middle Paleolithic. Journal of Human Evolution, 60(4): 437–451, even without invoking changes in annual mean precipitation.

is **not** designed to generate the exact lake level evolution of Lake Lisan, but rather to illustrate in a very idealized thought experiment the fact that even for reduced glacial precipitation, lake level can be considerably higher (lower) than for present-day conditions, if the glacial evaporation was reduced by an even larger (smaller) amount.

The lake level evolution of the two locations are shown in Fig. 12. The simulated and idealized Lisan Lake level evolution ($L_{DSB}(t)$) exhibits a steady increase from low levels around 50–60 kyr into the Last Glacial Maximum. Peak lake levels are attained around 16 ka followed by a steady Holocene decline of about 250 m. The P-E timeseries also documents that a tiny imbalance of about several centimeters per year (several percent of the mean evaporation rates) can accumulate on orbital timescales into considerable lake level anomalies of several hundred meters. Contrasting the glacial evolution of Lake Lisan, the idealized lake level simulation for Lake Van ($L_{Van}(t)$) exhibits declining lake levels from MIS5b to MIS2 and minimum values around 16 ka and a Holocene increase (Fig. 12A).

Thus, reduced MIS3 and MIS2 precipitation (consistent with speleothem hydroclimate data from the Levant region and PC1 of Lake Van; Fig. 11) can lead to either higher or, lower lake levels, depending on the delicately balanced relative changes in temperature-driven evaporation. Therefore, decreasing simulated and reconstructed glacial precipitation in the Eastern Mediterranean region is not inconsistent with the high glacial lake stands in DSB lakes. We find that although glacial evaporation and precipitation were both reduced for two locations compared to present-day, the model, for reasonable parameter values, can still simulate opposing glacial trajectories with lower LGM lake level for Lake Van (Fig. 12A) and higher one for Lake Lisan (Fig. 12B).

6. Summary

Our study presented a 360 kyr-long new color record from Lake Van showing DO variability with unprecedented decadal-scale resolution. The millennial-scale variability recorded by the ultra-high resolution color variations and changes in pollen percentages, TOC, CaCO$_3$, Si and K correspond to large-scale hydroclimate changes. Dansgaard-Oeschger and Heinrich stadials lead to massive drying of the Eastern Mediterranean and rapid shifts from aridity to pluvials are recorded for stadial/interstadial transitions. By combining individual hydroclimate-sensitive paleo-proxies from Lake Van using EOF analysis, we derived a combined hydroclimate index (PC1), which correlates well with precipitation changes simulated by a transient DO hindcast simulation performed with the LOVECLIM earth system model. From this simulation it is deduced that North Atlantic stadials, associated with a weaker AMOC, generate a massive anticyclonic circulation anomaly extending from northern Africa, the Mediterranean to Northern Europe and east into Central Asia. This large-scale circulation feature advects dry and cold continental air masses towards the Lake Van site, thus explaining the paleo-proxy evidence. The length of millennial-scale droughts tracks that of DO stadials. The most severe droughts in the Eastern Mediterranean are found when stadials and low precession coincide with the presence of large northern Hemisphere ice sheets, such as during MIS2.

Our statistical analysis of the PC1 record showed evidence for enhanced DO and millennial-scale activity during the presence of medium-sized ice-sheets. This supports the notion that conditions with maximum ice-sheet size can be regarded as extended stadials, with continuous freshwater background discharging into the North Atlantic and hence weaker AMOC. The near absence of millennial-scale activity in PC1 during interglacials points to the importance of ice-sheets in generating DO variability.

Analyzing the orbital-scale variability in the Lake Van

hydroclimate record we found that increasing precession leads to an enhancement of spring to early summer precipitation, as well as winter precipitation through the enhancement of the winter storm track. This situation enhances the mean annual rainfall considerably, as well as the seasonality between spring precipitation and late summer drought, as documented by the transient LOVECLIM model experiments and by the varved sections in the Lake Van record and their preferred occurrence during high precession phases. Such conditions were particularly pronounced during MIS5e, 5c, 5a.

Hydroclimate changes in the Eastern Mediterranean were also modulated on the 100 kyr ice-sheet/eccentricity timescale. The atmospheric response to the orographic forcing from the mature Laurentide and Eurasian ice-sheets caused enhanced subsidence in the western Mediterranean and an anomalous low pressure in the Eastern Mediterranean and Levant region, which advected dry air from northeastern Africa towards the Lake Van region.

The Lake Van hydroclimate reconstructions are a new member in a long list of records that shows large-scale glacial drying in the Levant and Eastern Mediterranean. Using a simplified lake level model, forced by the transient LOVECLIM simulations, we demonstrated that this finding is not necessarily inconsistent with higher Lake Lisan lake levels during this period, if for Lake Lisan a reduction of precipitation occurred in conjunction with an even stronger reduction in evaporation. However, based on our modeling experiments, a regional-scale anomaly for Lake Lisan cannot be excluded. LOVECLIM is a relatively coarse-resolution climate model, which does not capture the detailed small-scale responses that play a role for hydroclimate variability in eastern Turkey, Anatolia and the Levant. Nevertheless, the fact that our model simulates a realistic semi-annual cycle in rainfall under present-day conditions and the notion that millennial-scale and orbital-scale droughts are large-scale features, which are both reconstructed and simulated, supports the robustness of our model-based conclusions.

Methodologically, our study makes significant advances in combining transient climate model simulations with the Lake Van hydroclimate reconstructions. Statistical analysis relating to the Lake Van precipitation changes on millennial and orbital scales was made by directly regressing changes in PC1 reconstructions with simulated atmospheric data. The resulting patterns provided key insights into the atmospheric drivers of subtropical megadroughts. Furthermore we see from the high correlations between PC1 and the simulated orbital-scale rainfall changes in LOVECLIM, that the model simulations could have been used to generate an alternative age model for the paleo-climate data. Driven by atmospheric CO$_2$ concentrations (on EDC3), ice-sheet orography and orbital-forcings, the physical model simulates rainfall variability in eastern Turkey, which could have been used in conjunction with the multiproxy PC1 data to derive a physically-tuned age model. This idea, which relies on the dating of the external forcings, the realism of the model simulations and the interpretation of the paleo-proxy data, will be pursued in future studies.

and support and the Yüzüncü Yıl Üniversitesi of Van, Turkey for providing the infrastructure. AT. and T.F. are supported through the US NSF (grants ANT-1341311, 1010869) and L. M. acknowledges support from the Australian Research Council (grant DE150100107). The MIS3 and MIS2 transient LOVECLIM simulations were performed on a computational cluster owned by the Faculty of Science of the University of New South Wales. The reported data are available as Tables 1–6 in the Supplementary Information. The data for the transient LOVECLIM experiments can also be accessed through http://apdrc.soest.hawaii.edu/dods/public_data/Paleoclimate_modeling/LOVECLIM/800k and http://apdrc.soest.hawaii.edu/dods/public_data/Paleoclimate_modeling/LOVECLIM/Dansgaard-Oeschger.

Appendix A. Supplementary data

Supplementary data related to this article can be found at http://dx.doi.org/10.1016/j.quascirev.2015.12.016.

References

Abe-Ouchi, A., Segawa, T., Saito, F., 2007. Climatic Conditions for modelling the Northern Hemisphere ice sheets throughout the ice age cycle. Clim. Past 3 (3), 423–438.

Allen, J.R.M., Brandt, U., Brauer, A., Hubberten, H.W., Huntley, B., Keller, J., Kraml, M., Mackensen, A., Mingram, J., Negendank, J.F.W., Nowaczyk, N.R., Oberhansli, H., Watts, W.A., Wulf, S., Zolitschka, B., 1999. Rapid environmental changes in southern Europe during the last glacial period. Nature 400 (6746), 740–743.

Allen, J.R.M., Watts, W.A., Huntley, B., 2000. Weichselian palynostratigraphy, palaeovegetation and palaeoenvironment; the record from Lago Grande di Monticchio, southern Italy. Quat. Int. 73–74, 91–110.

Almogi-Labin, A., Bar-Matthews, M., Shriki, D., Kolosovsky, E., Paterne, M., Schilman, B., Ayalon, A., Aizenshtat, Z., Matthews, A., 2009. Climatic variability during the last 90 ka of the southern and northern Levantine Basin as evident from marine records and speleothems. Quat. Sci. Rev. 28 (25–26), 2882–2896.

Andersen, K., Azuma, N., Barnola, J., Bigler, M., Biscaye, P., Caillon, N., Chappellaz, J., Clausen, H., Dahl-Jensen, D., Fischer, H., Fluckiger, J., Fritzsche, D., Fujii, Y., Goto-Azuma, K., Gronvold, K., Gundestrup, N., Hansson, M., Huber, C., Hvidberg, C., Johnsen, S., Jonsell, U., Jouzel, J., Kipfstuhl, S., Landais, A., Leuenberger, M., Lorrain, R., Masson-Delmotte, V., Miller, H., Motoyama, H., Narita, H., Popp, T., Rasmussen, S., Raynaud, D., Röthlisberger, R., Ruth, U., Samyn, D., Schwander, J., Shoji, H., Siggard-Andersen, M., Steffensen, J., Stocker, T., Sveinbjörnsdóttir, A., Svensson, A., Takata, M., Tison, J., Thorsteinsson, T., Watanabe, O., Wilhelms, F., White, J., Project, N.G.I.C. 2004. High-resolution record of Northern Hemisphere climate extending into the last interglacial period. Nature 147–151.

Badertscher, S., Fleitmann, D., Cheng, H., Edwards, R.L., Gokturk, O.M., Zumbuhl, A., Leuenberger, M., Tuysuz, O., 2011. Pleistocene water intrusions from the Mediterranean and Caspian seas into the Black Sea. Nat. Geosci. 4 (4), 236–239.

Bar-Matthews, M., Ayalon, A., Gilmour, M., Matthews, A., Hawkesworth, C.J., 2003. Sea–land oxygen isotopic relationships from planktonic foraminifera and speleothems in the Eastern Mediterranean region and their implication for paleorainfall during interglacial intervals. Geochim. Cosmochim. Acta 67 (17), 3181–3199.

Barker, S., Knorr, G., Edwards, R.L., Parrenin, F., Putnam, A.E., Skinner, L.C., Wolff, E., Ziegler, M., 2011. 800,000 Years of abrupt climate variability. Science 334 (6054), 347–351.

Bartov, Y., Goldstein, S., Stein, M., Enzel, Y., 2003. Catastrophic arid episodes in the Eastern Mediterranean linked with the North Atlantic Heinrich events. Geology 439–442.

Berger, A., 1978. Long-term variations of caloric insolation resulting from the earth's orbital elements. Quat. Res. 9 (2), 139–167.

Bonacci, O., 2001. Analysis of the maximum discharge of karst springs. Hydrogeol. J. 9 (4), 328–338.

Bond, G., Broecker, W., Johnsen, S., McManus, J., Labeyrie, L., Jouzel, J., Bonani, G., 1993. Correlations between climate records from North-Atlantic sediments and Greenland Ice. Nature 365 (6442), 143–147.

Brovkin, V., Ganopolski, A., Svirezhev, Y., 1997. A continuous climate-vegetation classification for use in climate-biosphere studies. Ecol. Model. 101 (2–3), 251–261.

Capron, E., Landais, A., Chappellaz, J., Schilt, A., Buiron, D., Dahl-Jensen, D., Johnsen, S.J., Jouzel, J., Lemieux-Dudon, B., Loulergue, L., Leuenberger, M., Masson-Delmotte, V., Meyer, H., Oerter, H., Stenni, B., 2010. Millennial and sub-millennial scale climatic variations recorded in polar ice cores over the last glacial period. Clim. Past 6 (3), 345–365.

Cheng, H., Edwards, R.L., Broecker, W.S., Denton, G.H., Kong, X.G., Wang, Y.J., Zhang, R., Wang, X.F., 2009. Ice age terminations. Science 326 (5950), 248–252.

Chester, P.I., Rains, J.I., 2001. Pollen and spore keys for Quaternary deposits in the northern Pindos Mountains, Greece. Grana 40 (6), 299–387.

Cukur, D., Krastel, S., Schmincke, H.U., Sumita, M., Çağatay, N., Meydan, A.F., Damcı, E., Stockhecke, M., 2014. Seismic stratigraphy of Lake Van, eastern Turkey. Quat. Sci. Rev. 104, 63–84.

Daniau, A.L., Sanchez-Goni, M.F., Beaufort, L., Laggoun-Defarge, F., Loutre, M.F., Duprat, J., 2007. Dansgaard-Oeschger climatic variability revealed by fire emissions in southwestern Iberia. Quat. Sci. Rev. 26 (9–10), 1369–1383.

Dee, D.P., Uppala, S.M., Simmons, A.J., Berrisford, P., Poli, P., Kobayashi, S., Andrae, U., Balmaseda, M.A., Balsamo, G., Bauer, P., Bechtold, P., Beljaars, A.C.M., van de Berg, L., Bidlot, J., Bormann, N., Delsol, C., Dragani, R., Fuentes, M., Geer, A.J., Haimberger, L., Healy, S.B., Hersbach, H., Holm, E.V., Isaksen, L., Kallberg, P., Kohler, M., Matricardi, M., McNally, A.P., Monge-Sanz, B.M., Morcrette, J.J., Park, B.K., Peubey, C., de Rosnay, P., Tavolato, C., Thepaut, J.N., Vitart, F., 2011. The ERA-Interim reanalysis: configuration and performance of the data assimilation system. Q. J. R. Meteorol. Soc. 137 (656), 553–597.

Deplazes, G., Luckge, A., Peterson, L.C., Timmermann, A., Hamann, Y., Hughen, K.A., Rohl, U., Laj, C., Cane, M.A., Sigman, D.M., Haug, G.H., 2013. Links between tropical rainfall and North Atlantic climate during the last glacial period. Nat. Geosci. 6 (3), 213–217.

Develle, A.L., Gasse, F., Vidal, L., Williamson, D., Demory, F., Van Campo, E., Ghaleb, B., Thouveny, N., 2011. A 250 ka sedimentary record from a small karstic lake in the northern Levant (Yammoûneh, Lebanon). Paleogeogr. Paleoclimatol. Paleoecol 305, 10–27.

Drysdale, R.N., Zanchetta, G., Hellstrom, J.C., Fallick, A.E., Zhao, J.X., 2005. Stalagmite evidence for the onset of the Last Interglacial in southern Europe at 129 +/- 1 ka. Geophys. Res. Lett. 32 (24).

Enzel, Y., Arnit, R., Dayan, U., Crouvi, O., Kahana, R., Ziv, B., Sharon, D., 2008. The climatic and physiographic controls of the eastern Mediterranean over the late Pleistocene climates in the southern Levant and its neighboring deserts. Glob. Planet. Change 60 (3–4), 165–192.

Eshel, G., Farrell, B.F., 2000. Mechanisms of eastern Mediterranean rainfall variability. J. Atmos. Sci. 57 (19), 3219–3232.

Fleitmann, D., Cheng, H., Badertscher, S., Edwards, R.L., Mudelsee, M., Goekturk, O.M., Fankhauser, A., Pickering, R., Raible, C.C., Matter, A., Kramers, J., Tuysuz, O., 2009. Timing and climatic impact of Greenland interstadials recorded in stalagmites from northern Turkey. Geophys. Res. Lett. 36.

Fletcher, W.J., Muller, U.C., Koutsodendris, A., Christanis, K., Pross, J., 2013. A centennial-scale record of vegetation and climate variability from 312 to 240 ka (Marine Isotope Stages 9c-a, 8 and 7e) from Tenaghi Philippon, NE Greece. Quat. Sci. Rev. 78, 108–125.

Frumkin, A., Bar-Yosef, O., Schwarcz, H.P., 2011. Possible paleohydrologic and paleoclimatic effects on hominin migration and occupation of the Levantine Middle Paleolithic. J. Hum. Evol. 60 (4), 437–451.

Gasse, F., Vidal, L., Van Campo, E., Demory, F., Develle, A.-L., Tachikawa, K., Elias, A., Bard, E., Garcia, M., Sonzogni, C., Thouveny, N., 2015. Hydroclimatic changes in northern Levant over the past 400,000 years. Quat. Sci. Rev. 111 (0), 1–8.

Ganopolski, A., Calov, R., 2011. The role of orbital forcing, carbon dioxide and regolith in 100 kyr glacial cycles. Clim. Past 7 (4), 2391–2411.

Goosse, H., Brovkin, V., Fichefet, T., Haarsma, R., Huybrechts, P., Jongma, J., Mouchet, A., Selten, F., Barriat, P.Y., Campin, J.M., Deleersnijder, E., Driesschaert, E., Goelzer, H., Janssens, I., Loutre, M.F., Morales Maqueda, M.A., Opsteegh, T., Mathieu, P.P., Munhoven, G., Pettersson, E.J., Renssen, H., Roche, D.M., Schaeffer, M., Tartinville, B., Timmermann, A., Weber, S.L., 2010. Description of the Earth system model of intermediate complexity LOVECLIM version 1.2. Geosci. Model Dev. 3 (2), 603–633.

Goosse, H., Fichefet, T., 1999. Importance of ice-ocean interactions for the global ocean circulation: a model study. J. Geophys. Res. 104 (C10), 23337–23355.

Grützner, J., Higgins, S.M., 2010. Threshold behavior of millennial scale variability in deep water hydrography inferred from a 1.1 Ma long record of sediment provenance at the southern Gardar Drift. Paleoceanography 25 (4), PA4204.

Harrison, S.P., Goñi, M.F.S., 2010. Global patterns of vegetation response to millennial-scale variability and rapid climate change during the last glacial period. Quat. Sci. Rev. 29 (21–22), 2957–2980.

Hemming, S.R., 2004. Heinrich events: massive late pleistocene detritus layers of the North Atlantic and their global climate imprint. Rev. Geophys. 42 (1), RG1005.

Hodell, D., Crowhurst, S., Skinner, L., Tzedakis, P.C., Margari, V., Channell, J.E.T., Kamenov, G., Maclachlan, S., Rothwell, G., 2013. Response of Iberian Margin sediments to orbital and suborbital forcing over the past 420 ka. Paleoceanography 28 (1).

Hodell, D.A., Channell, J.E.T., Curtis, J.H., Romero, O.E., Röhl, U., 2008. Onset of "Hudson Strait" Heinrich events in the eastern North Atlantic at the end of the middle Pleistocene transition (~640 ka)? Paleoceanography 23 (4), PA4218.

Jansen, J.H.F., Van der Gaast, S.J., Koster, B., Vaars, A.J., 1998. Short communication CORTEX, a shipboard XRF-scanner for element analyses in split sediment cores. Mar. Geol. 145–153.

Jouzel, J., Masson-Delmotte, V., Cattani, O., Dreyfus, G., Falourd, S., Hoffmann, G., Minster, B., Nouet, J., Barnola, J.M., Chappellaz, J., Fischer, H., Gallet, J.C., Johnsen, S., Leuenberger, M., Loulergue, L., Luethi, D., Oerter, H., Parrenin, F., Raisbeck, G., Raynaud, D., Schilt, A., Schwander, J., Selmo, E., Souchez, R., Spahni, R., Stauffer, B., Steffensen, J.P., Stenni, B., Stocker, T.F., Tison, J.L., Werner, M., Wolff, E.W., 2007. Climate variability over the past 800 000 years. Science 317, 793.

Kaden, H., Peeters, F., Lorke, A., Kipfer, R., Tomonaga, Y., Karabiyikoglu, M., 2010. Impact of lake level change on deep-water renewal and oxic conditions in deep saline Lake Van, Turkey. Water Resour. Res. 46.

Kadioglu, M., Sen, Z., Batur, E., 1997. The greatest soda-water lake in the world and how it is influenced by climatic change. Ann. Geophys. Atmos. Hydrospheres Space Sci. 15 (11), 1489—1497.

Kroon, D., Alexander, I., Little, M., Lourens, L.J., Matthewson, A., Robertson, A.H.F., Sakamoto, T., 1998. Oxygen isotope and sapropel stratigraphy in the Eastern Mediterranean during the last 3.2 million years. In: Proceedings of the ODP Scientific Results, pp. 181—190.

Kutzbach, J.E., Chen, G., Cheng, H., Edwards, R.L., Liu, Z., 2014. Potential role of winter rainfall in explaining increased moisture in the Mediterranean and Middle East during periods of maximum orbitally-forced insolation seasonality. Clim. Dyn. 42 (3—4), 1079—1095.

Kuzucuoglu, C., Christol, A., Mouralis, D., Dogu, A.F., Akkoprou, E., Fort, M., Brunstein, D., Zorer, H., Fontugne, M., Karabiyikoglu, M., Scaillet, S., Reyss, J.L., Guillou, H., 2010. Formation of the Upper Pleistocene terraces of Lake Van (Turkey). J. Quat. Sci. 25 (7), 1124—1137.

Kwiecien, O., Stockhecke, M., Pickarski, Nadine, Litt, T., Sturm, M., Anselmetti, F., Haug, G.H., 2014. Dynamics of the last four glacial terminations recorded in Lake Van, Turkey. Quat. Sci. Rev. 104, 42—52.

Lazar, B., Sivan, O., Yechieli, Y., Levy, E.J., Antler, G., Gavrieli, I., Stein, M., 2014. Long-term freshening of the Dead Sea brine revealed by porewater Cl− and d18O in ICDP Dead Sea deep-drill. Earth Planet. Sci. Lett. 400, 94—101.

Lemcke, G., 1996. Paläoklimarekonstruktion Am Van See (Ostanatolien, Türkei) (PhD thesis). Swiss Federal Institute of Technology Zurich. ETH, p. 182.

Lisiecki, L.E., Raymo, M.E., 2005. A Pliocene-Pleistocene stack of 57 globally distributed benthic δ18O records. Paleoceanography 20, PA1003 (Data archived at the World Data Center for Paleoclimatology, Boulder, Colorado, USA).

Litt, T., Anselmetti, F.S., Baumgarten, H., Beer, J., Cagatay, N., Cukur, D., Damci, E., Glombitza, C., Heumann, G., Kallmeyer, J., Kipfer, R., Krastel, S., Kwiecien, O., Meydan, A.F., Orcen, S., Pickarski, N., Randlett, M.-E., Schmincke, H.-U., Schubert, C.J., Sturm, M., Sumita, M., Stockhecke, M., Tomonaga, Y., Vigliotti, L., Wonik, T., 2012. 500,000 years of environmental history in eastern Anatolia: the PALEOVAN Drilling Project. Sci. Drill. 18—29.

Litt, T., Pickarski, N., Heumann, G., Stockhecke, M., Tzedakis, P., 2014. A 600,000 year long continental pollen record from Lake Van, eastern Anatolia (Turkey). Quat. Sci. Rev. 104, 30—41.

Martrat, B., Grimalt, J.O., Shackleton, N.J., de Abreu, L., Hutterli, M.A., Stocker, T.F., 2007. Four climate cycles of recurring deep and surface water destabilizations on the Iberian margin. Science 317 (5837), 502—507.

McManus, J.F., Oppo, D.W., Cullen, J.L., 1999. A 0.5-million-year record of millennial-scale climate variability in the North Atlantic. Science 283 (5404), 971—975.

Menviel, L., Timmermann, A., Friedrich, T., England, M.H., 2014. Hindcasting the continuum of Dansgaard-Oeschger variability: mechanisms, patterns and timing. Clim. Past 10 (1), 63—77.

Menviel, L., Timmermann, A., Timm, O.E., Mouchet, A., 2011. Deconstructing the Last Glacial termination: the role of millennial and orbital-scale forcings. Quat. Sci. Rev. 30 (9—10), 1155—1172.

Muller, U.C., Pross, J., Tzedakis, P.C., Gamble, C., Kotthoff, U., Schmiedl, G., Wulf, S., Christanis, K., 2011. The role of climate in the spread of modern humans into Europe. Quat. Sci. Rev. 30 (3—4), 273—279.

Neugebauer, I., Brauer, A., Schwab, M.J., Waldmann, N., Enzel, Y., Kitagawa, H., Torfstein, A., Frank, U., Dulski, P., Agnon, A., Ariztegui, D., Ben-Avraham, Z., Goldstein, S.L., Stein, M., 2014. Lithology of the long sediment record recovered by the ICDP Dead Sea Deep Drilling Project (DSDDP). Quat. Sci. Rev. 102, 149—165.

Opsteegh, J.D., Haarsma, R.J., Selten, F.M., Kattenberg, A., 1998. ECBILT: a dynamic alternative to mixed boundary conditions in ocean models. Tellus A 50 (3), 348—367.

Peeters, F., Kipfer, R., Achermann, D., Hofer, M., Aeschbach-Hertig, W., Beyerle, U., Imboden, D.M., Rozanski, K., Frohlich, K., 2000. Analysis of deep-water exchange in the Caspian Sea based on environmental tracers. Deep Sea Res. Part I Oceanogr. Res. Pap. 47 (4), 621—654.

Penaud, A., Eynaud, F., Sanchez-Goñi, M., Malaize, B., Turon, J.L., Rossignol, L., 2011. Contrasting sea-surface responses between the western Mediterranean Sea and eastern subtropical latitudes of the North Atlantic during abrupt climatic events of MIS 3. Mar. Micropaleontol. 80 (1—2), 1—17.

Rasmussen, S.O., Andersen, K.K., Svensson, A.M., Steffensen, J.P., Vinther, B.M., Clausen, H.B., Siggaard-Andersen, M.L., Johnsen, S.J., Larsen, L.B., Dahl-Jensen, D., Bigler, M., Röthlisberger, R., Fischer, H., Goto-Azuma, K., Hansson, M.E., Ruth, U., 2006. A new Greenland ice core chronology for the last glacial termination. J. Geophys. Res. 111 (D6), D06102.

Reille, M., 1990. Lecons de Palynologie et d'Analyse Pollinique. Editions du Centre Nacional de la Recherche Scientifique (CNRS), Paris.

Reille, M., 1992. Pollen et Spores d'Europe et d'Afrique du Nord. Laboratoire de Botanique Historique et Palynologie. URA CNRS, Marseille.

Reille, M., 1995. Pollen et Spores d'Europe et d'Afrique du Nord. Suppl. 1. In: Laboratoire de Botanique Historique et Palynologie. URA CNRS, Marseille.

Reille, M., 1998. Pollen et Spores d'Europe et d'Afrique du Nord. Suppl. 2. Laboratoire de Botanique Historique et Palynologie. URA CNRS, Marseille.

Rodwell, M.J., Hoskins, B.J., 1996. Monsoons and the dynamics of deserts. Q. J. R. Meteorol. Soc. 122 (534), 1385—1404.

Rohling, E.J., 2013. Quantitative assessment of glacial fluctuations in the level of Lake Lisan, Dead Sea rift. Quat. Sci. Rev. 70, 63—72.

Rosenberg, T.M., Preusser, F., Risberg, J., Plikk, A., Kadi, K.A., Matter, A., Fleitmann, D., 2013. Middle and Late Pleistocene humid periods recorded in palaeolake deposits of the Nafud desert, Saudi Arabia. Quat. Sci. Rev. 70, 109—123.

Rowe, P.J., Mason, J.E., Andrews, J.E., Marca, A.D., Thomas, L., van Calsteren, P., Jex, C.N., Vonhof, H.B., Al-Omari, S., 2012. Speleothem isotopic evidence of winter rainfall variability in northeast Turkey between 77 and 6 ka. Quat. Sci. Rev. 45, 60—72.

Schulz, M., 2002. The tempo of climate change during Dansgaard-Oeschger interstadials and its potential to affect the manifestation of the 1470-year climate cycle. Geophys. Res. Lett. 29 (1).

Stein, M., Torfstein, A., Gavrieli, I., Yechieli, Y., 2010. Abrupt aridities and salt deposition in the post-glacial Dead Sea and their North Atlantic connection. Quat. Sci. Rev. 29 (3—4), 567—575.

Stein, M., Starinsky, A., Katz, A., Goldstein, S.L., Machlus, M., Schramm, A., 1997. Strontium isotopic, chemical, and sedimentological evidence for the evolution of Lake Lisan and the Dead Sea. Geochim. Cosmochim. Acta 61, 3975—3992.

Stevens, L.R., Djamali, M., Andrieu-Ponel, V., de Beaulieu, J.L., 2012. Hydroclimatic variations over the last two glacial/interglacial cycles at Lake Urmia, Iran. J. Paleolimnol. 47 (4), 645—660.

Stockhecke, M., 2013. Exploring the 600,000 Year Old Sedimentary Record of Lake Van (Turkey): Lithostratigraphy, Chronology and Hydroclimate Reconstruction. ETH, Zurich (Dissertation).

Stockhecke, M., Anselmetti, F.S., Meydan, A.F., Odermatt, D., Sturm, M., 2012. The annual particle cycle in Lake Van (Turkey). Palaeogeogr. Palaeoclimatol. Palaeoecol. 333, 148—159.

Stockhecke, M., Kwiecien, O., Vigliotti, L., Anselmetti, F., Beer, J., Çağatay, N., Channell, J.E.T., Kipfer, R., Lachner, J., Litt, T., Pickarski, N., Sturm, M., 2014a. Chronostratigraphy of the 600,000 year old continental record of Lake Van (Turkey). Quat. Sci. Rev. 104, 8—17.

Stockhecke, M., Sturm, M., Brunner, I., Schmincke, H.-U., Sumita, M., Cukur, D., Kwiecien, O., Anselmetti, F., 2014b. Sedimentary evolution and environmental history of Lake Van (Turkey) over the past 600 000 years. Sedimentology 61 (6), 1830—1861.

Sumita, M., Schmincke, H.U., 2013. Impact of volcanism on the evolution of Lake Van II: temporal evolution of explosive volcanism of Nemrut Volcano (eastern Anatolia) during the past ca. 0.4 Ma. J. Volcanol. Geotherm. Res. 253, 15—34.

Svensson, A., Andersen, K.K., Bigler, M., Clausen, H.B., Dahl-Jensen, D., Davies, S.M., Johnsen, S.J., Muscheler, R., Parrenin, F., Rasmussen, S.O., Röthlisberger, R., Seierstad, I., Steffensen, J.P., Vinther, B.M., 2008. A 60 000 year Greenland stratigraphic ice core chronology. Clim. Past 4 (1), 47—57.

Timm, O., Köhler, P., Timmermann, A., Menviel, L., 2010. Mechanisms for the onset of the African Humid Period and Sahara greening 14.5-11 ka BP. J. Clim. 23 (10), 2612—2633.

Timm, O., Timmermann, A., 2007. Simulation of the last 21000 years using accelerated transient boundary conditions. J. Clim. 20 (17), 4377—4401.

Timm, O., Timmermann, A., Abe-Ouchi, A., Saito, F., Segawa, T., 2008. On the definition of seasons in paleoclimate simulations with orbital forcing. Paleoceanography 23 (2), PA2221.

Timmermann, A., Friedrich, T., Timm, O.E., Chikamoto, M.O., Abe-Ouchi, A., Ganopolski, A., 2014. Modeling obliquity and CO2 effects on Southern Hemisphere Climate during the past 408 ka. J. Clim. 27 (5), 1863—1875.

Timmermann, A., Knies, J., Timm, O.E., Abe-Ouchi, A., Friedrich, T., 2010. Promotion of glacial ice sheet buildup 60—115 kyr B.P. by precessionally paced Northern Hemispheric meltwater pulses. Paleoceanography 25 (4), PA4208.

Torfstein, A., Goldstein, S.L., Stein, M., Kushnir, Y., Enzel, Y., Haug, G., 2015. Dead Sea drawdown and monsoonal impacts in the Levant during the Last Interglacial. Earth Planet. Sci. Lett. 412, 235—244.

Torfstein, A., Goldstein, S.L., Stein, M., Enzel, Y., 2013. Impacts of abrupt climate changes in the Levant from Last Glacial Dead Sea levels. Quat. Sci. Rev. 69, 1—7.

Torfstein, A., Haase-Schramm, A., Waldmann, N., Kolodny, Y., Stein, M., 2009. U-series and oxygen isotope chronology of the mid-Pleistocene Lake Amora (Dead Sea basin). Geochim. Cosmochim. Acta 73 (9), 2603—2630.

Tzedakis, P.C., 1994. Vegetation change through glacial-interglacial cycles — a long pollen sequence perspective. Philos. Trans. R. Soc. Lond. Ser. B Biol. Sci. 345 (1314), 403—432.

Tzedakis, P.C., 2007. Seven ambiguities in the Mediterranean palaeoenvironmental narrative. Quat. Sci. Rev. 26 (17—18), 2042—2066.

Tzedakis, P.C., Hooghiemstra, H., Palike, H., 2006. The last 1.35 million years at Tenaghi Philippon: revised chronostratigraphy and long-term vegetation trends. Quat. Sci. Rev. 25 (23—24), 3416—3430.

Vaks, A., Bar-Matthews, M., Matthews, A., Ayalon, A., Frumkin, A., 2010. Middle-Late Quaternary paleoclimate of northern margins of the Saharan-Arabian Desert: reconstruction from speleothems of Negev Desert, Israel. Quat. Sci. Rev. 29 (19—20), 2647—2662.

van Kreveld, S., Sarnthein, M., Erlenkeuser, H., Grootes, P., Jung, S., Nadeau, M.J., Pflaumann, U., Voelker, A., 2000. Potential links between surging ice sheets, circulation changes, and the Dansgaard-Oeschger cycles in the Irminger Sea, 60-18 kyr. Paleoceanography 15 (4), 425—442.

Van Meerbeeck, C.J., Renssen, H., Roche, D.M., Wohlfarth, B., Bohncke, S.J.P., Bos, J.A.A., Engels, S., Helmens, K.F., Sanchez-Goni, M.F., Svensson, A., Vandenberghe, J., 2011. The nature of MIS 3 stadial-interstadial transitions in Europe: new insights from model-data comparisons. Quat. Sci. Rev. 30 (25—26), 3618—3637.

Van Zeist, W., Woldring, H., 1978. A postglacial pollen diagram from Lake Van in East Anatolia. Rev. Palaeobot. Palynol. 249—276.

Veres, D., Bazin, L., Landais, A., Kele, H.T.M., Lemieux-Dudon, B., Parrenin, F., Martinerie, P., Blayo, E., Blunier, T., Capron, E., Chappellaz, J., Rasmussen, S.O., Severi, M., Svensson, A., Vinther, B., Wolff, E.W., 2013. The Antarctic ice core

chronology (AICC2012): an optimized multi-parameter and multi-site dating approach for the last 120 thousand years. Clim. Past 9 (4), 1733—1748.

Vogel, H., Wagner, B., Zanchetta, G., Sulpizio, R., Rosen, P., 2010. A paleoclimate record with tephrochronological age control for the last glacial-interglacial cycle from Lake Ohrid, Albania and Macedonia. J. Paleolimnol. 44 (1), 295—310.

Waelbroeck, C., Labeyrie, L., Michel, E., Duplessy, J.C., McManus, J.F., Lambeck, K., Balbon, E., Labracherie, M., 2002. Sea-level and deep water temperature changes derived from benthic foraminifera isotopic records. Quat. Sci. Rev. 21 (1—3), 295—305.

Waldmann, N., Stein, M., Ariztegui, D., Starinsky, A., 2009. Stratigraphy, depositional environments and level reconstruction of the last interglacial Lake Samra in the Dead Sea basin. Quat. Res. 72 (1), 1—15.

Waldmann, N., Torfstein, A., Stein, M., 2010. Northward intrusions of low- and mid-latitude storms across the Saharo-Arabian belt during past interglacials. Geology 38 (6), 567—570.

Wolff, E.W., Chappellaz, J., Blunier, T., Rasmussen, S.O., Svensson, A., 2010. Millen-nial-scale variability during the last glacial: the ice core record. Quat. Sci. Rev. 29 (21—22), 2828—2838.

Zhao, Y.L., Liu, Z.F., Colin, C., Paterne, M., Siani, G., Cheng, X.R., Duchamp-Alphonse, S., Xie, X., 2011. Variations of the Nile suspended discharges during the last 1.75 Myr. Palaeogeogr. Palaeoclimatol. Palaeoecol. 311 (3—4), 230—241.